# Investigating the Effect of Dilatancy on Melt Segregation in Deforming Partially Molten Rock Using Dedalus


Andras G. Cserep

Exeter College

University of Oxford


Thesis to be submitted for the degree of

*Master of Earth Sciences*

Trinity Term 2025

Word Count: 7980

*Supervised by Professor Richard Katz and Dr Yuan Li*

**Abstract**

Partially molten rock is widely understood to be a melt-saturated, granular medium. However, the effect of granular interactions has rarely been incorporated into its modelling. This study explores the role of dilatancy in concentrating partial melts into low-angle bands. Strain-evolving models of simple shear and Poiseuille flow based on the framework set out by Katz et al. (2024) are developed. It is found that dilatancy can account for the low angles of melt-rich bands and the segregation of melts toward magmatic intrusion margins. However, it fails to recreate the characteristic band widths and spacings observed in experiments. It is concluded that the inclusion of the dilatant stresses is essential for accurately describing the rheology of partially molten rock. Future models should look to take into consideration the effects of grain-scale physics that can prevent bands forming at very high frequencies.

The simulations were implemented using Dedalus, a partial differential equation solver that uses spectral methods. Its effectiveness is evaluated for geophysical fluid dynamics research.

# Contents

# 1 Introduction

Partially molten rock (PMR) is a melt-saturated, granular medium (Katz et al., 2024). It is present in the asthenosphere, magmatic intrusions and under mid-ocean ridges, transporting momentum and chemical components between the Earth's solid mantle and its surface. This material plays a crucial role in mantle convection, magmatism, and the formation of new crust. Therefore, if we want to understand these processes, it is essential that the rheological properties of two-phase flows are accounted for.

## 1.1 Introduction to Melt Segregation

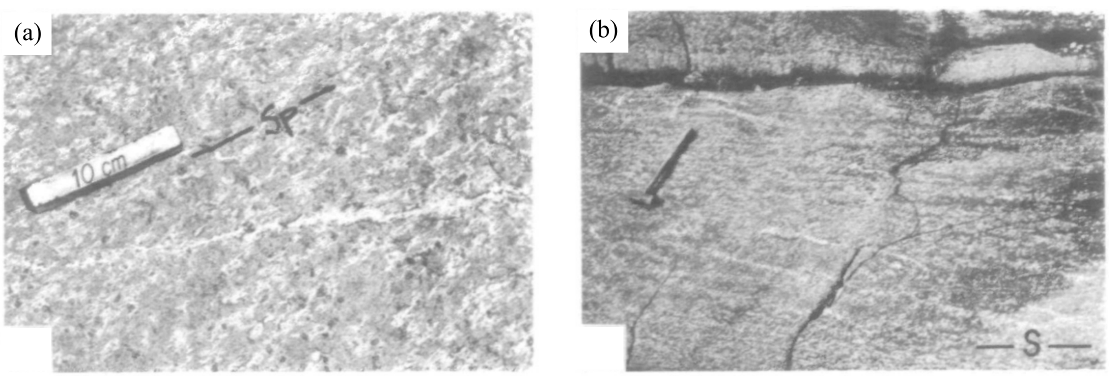


Figure 1: Field photos of dykes in (a) Liguria and (b) Lanzo showing the segregation of feldspathic melt in lenses parallel to sub-parallel to the peridotite flow plane. Around the lenses, there are melt depleted zones. Adapted from Nicholas (1986).

The enrichment of crustal rocks in incompatible elements relative to mantle xenoliths provides compelling evidence that Earth's outer layer is a product of its interior (Hofmann, 1988). PMR rheology must facilitate mechanisms for melt to segregate from the solid matrix and generate pathways for the extracted liquid to travel from the deeper mantle to the surface to create new crust. Such networks have been evidenced by seismic studies that show sheets of melt beneath rifts, orientated parallel to spreading centres (Kendall et al., 2005; Pilidou et al., 2005), dyke and mantle peridotite outcrops (Quick, 1981; Nicolas and Jackson, 1982; Nicolas, 1986) (Figure 1), as well as laboratory experiments on deforming olivine aggregates

(Beeman and Kohlstedt, 1993). The field studies demonstrated that melt can localise tens of kilometres below the Earth's surface during deformation and recognised the importance of permeability between regions of greater porosity, such as veins, for accelerating fluid flow (Quick, 1981; Nicolas and Jackson, 1982; Nicolas, 1986). Stevenson (1989), elaborated on this principle, suggesting that an increased fraction of melt could 'soften' PMR, reducing its shear viscosity. This mechanism was predicted to enhance melt migration in these regions, localising melt parallel to the minimum compressive stress from shearing, forming lenses at 45° to the shear planes.

To test this theory, several laboratory experiments have been carried out. The methodology outlined here is based on the studies by Holtzman et al. (2003, 2007) and Kohlstedt & Holtzman (2009). PMR is simulated by creating an aggregate of 95-98% olivine grains, mixed with smaller percentages of lower melting point materials, such as mid-ocean ridge basalts and chromium. The olivine grains typically have a mean diameter of $\sim 10\mu$m but may vary in size within a sample. After hydrostatically hot pressing the samples to remove gas bubbles, they are placed under a confining pressure of 300 MPa and heated to 1225°C. This is sufficient to melt the secondary minerals but preserve the solid olivine matrix to create a simulant of PMR at 10 km depth with an initial porosity of 2-5%. These are deformed using triaxial presses and are subsequently quenched for analysis. To gain a full understanding of the dynamics, experiments that simulate simple shear and torsional shear are carried out. Rheologies derived experimentally and mathematically must explain observations from both configurations to be considered representative of PMR (Figure 2).

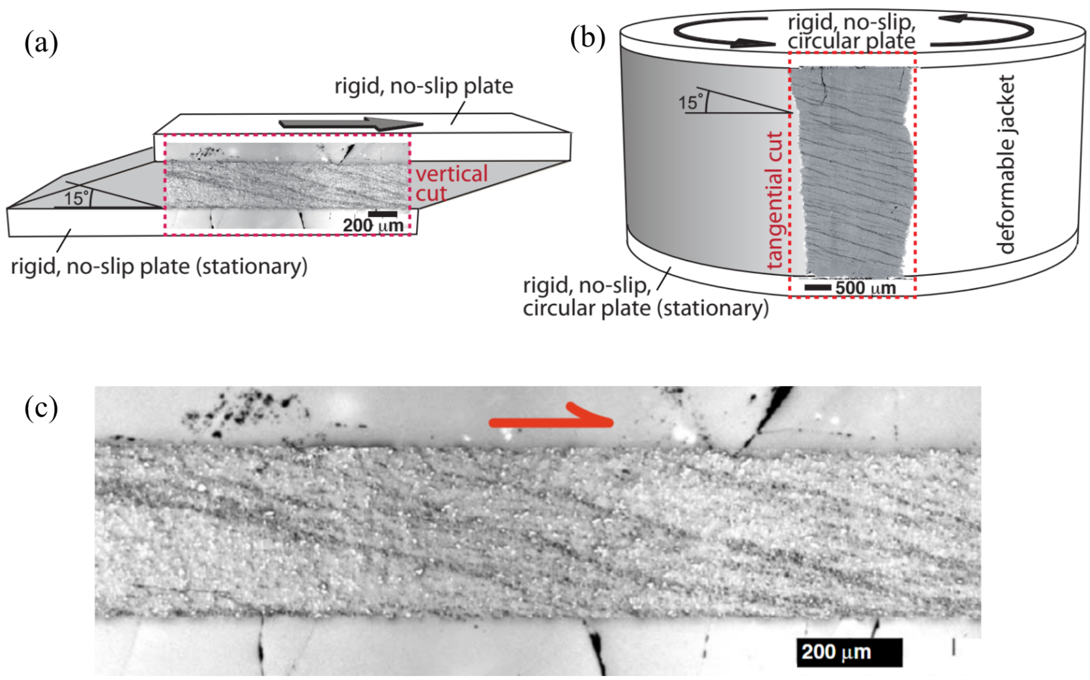


Figure 2: Quenched experiments of shearing partially molten rocks modified from Yasuko and Katz (2013). (a) and (c) show the results of a simple shear experiment by Holtzman and Kohlstedt (2007) showing black low-angle bands rich in melt after being sheared. (b) shows similar low-angle bands formed by a torsion experiment (King et al., 2010). Torsion experiments also record melt migration towards the central rotation axis.

The first study to explicitly test Stevenson's theory was Holtzman et al. (2003). Their results showed PMR can produce melt-segregated sheets 15-20° from a shearing plane, given that pressure gradients and the compaction length, the scale over which the melt flow and solid deformation are coupled (McKenzie, 1984), are smaller than the sample size. However, the latter requirement is not explained by classical PMR theory (McKenzie, 1984). Traditional thought suggests that the compaction length would only determine the maximum size of band growth, as segregation can only occur if melt and solid phases are coupled. This contradiction is justified by emphasising the role of short compaction lengths in limiting fluid flows that equilibrate pressure gradients within the samples (Holtzman et al., 2003). Consequently, they play an important role in facilitating the development of local pressure gradients that drive melt redistribution and form bands. The study also highlighted a discrepancy between the predicted band angles proposed by Stevenson (1989) and experimental observations. In a brief attempt to explain this, they call attention to the greater shear strains recorded within bands, indicating a level of localisation and partitioning. Stevenson's analysis did not include this detail and assumed a constant strain rate. Holtzman et al. (2003) argue that this could give rise to a balance between the angle of greatest band growth, at 45°, and maximum strain partitioning, parallel to the shear planes, forming bands at a compromise of 15-20°. It was further proposed that maintaining these low-angle bands over a range of strains from 1.1 to 5 likely requires a source of nonlinearity in the system that reinforces band growth at shallow angles instead of allowing them to be passively advected by the background shear.

The notion that bands concentrate shear was further explored by Katz et al. (2006). Since it is well known that mantle minerals can deform by power-law creep at high temperatures and dislocation climb at moderate stresses, it could be assumed that PMR has an effectively non-Newtonian rheology that would be able to concentrate strain and melts into bands. However, the power-law exponent of the shear viscosity required to localise the melts at 15-20° ($\mathfrak{n} \sim 4$–$6$) are much greater than that measured by King et al. (2010) to be at $1.5 \pm 0.3$ with 95% confidence, an almost Newtonian rheology. The theory was further contested by laboratory experiments in Newtonian diffusion creep regimes that also produced bands (Rudge and Bercovici, 2015) and for its inability to reproduce the migration of fluids towards the central axis seen in torsion experiments (Qi et al., 2015).

To address these challenges, numerous papers have sought to connect the observations from torsion experiments with Newtonian rheologies, primarily by relating grain-scale processes to the bulk properties of PMR. Takei and Holtzman (2009) suggested that the resistance to deformation is reduced in the direction of minimum contiguity, where the contact areas between neighbouring grains are at their lowest, resulting in the creation of melt bands. However, low-angle bands only formed when the contiguity tensor aligned with the principal stress directions, creating inherent viscous anisotropy (Takei and Katz, 2013). This is in contention with the experimental findings that calculate a misalignment of 15° between the contiguity tensor and principal stress direction (Qi et al., 2015; Qi et al., 2018).

Granular interactions are also affected by grain shape. Bercovici and Rudge (2015) identified that grains can undergo two forms of damage: interface damage, which reduces grain roughness, and void-generating damage, which only reduces resistance to compaction. As the latter cannot account for the non-linearity in effective shear viscosity, it cannot play a dominant role in porosity band emergence. However, by reducing roughness, interface damage can allow grains to slide over each other more easily and provide sharper pinning surfaces that hinder grain size growth. This results in smaller, weaker grains that enable more strain localisation and diffusion creep. However, grain size growth in PMR is poorly understood. Therefore, it is difficult to assess the effectiveness of this mechanism in strain-evolving numerical models. There is no literature to suggest that interface damage can reproduce the melt migration under torsion.

Another major consideration regarding the origin of porosity bands is their characteristic width and separation. Stevenson (1989) concludes that the separation will be some fraction of the compaction length and the aforementioned studies do not predict a minimum frequency for band formation (Katz et al., 2024). These ideas fail to adequately explain the experimental data, which shows distinct bands forming at separations around an order of magnitude greater than their widths (Holtzman et al., 2003).

Takei and Hier-Hajumder (2009) incorporated both the compaction and decompaction of the solid matrix with changes in the melt fraction due to dissolution and precipitation into their models. They argue that the latter processes are driven by interfacial tension, the cohesive force between particles and grains, creating a chemical gradient. This occurs on length scales smaller than the compaction length, called the diffusion length: the distance under which the melt fraction evolves primarily by diffusion. The wavelength of the perturbation in porosity determines which process is more dominant in driving melt transport. Shorter wavelength perturbations and smaller grain-sized regions are primarily controlled by local dissolution and precipitation (King, Hier-Majumder and Kohlstedt, 2011). This acts against melt segregation as the interfacial energy, which drives the interfacial tension, tries to reach a minimum by smoothing out heterogeneities, resulting in homogenisation. Such processes are known to occur after experiments are left to anneal post-shearing (Parsons et al., 2008). Thus, a lower limit of band wavelength can be determined where the negative growth rate from homogenisation is greater in magnitude than the decompaction-driven band growth rate from shear.

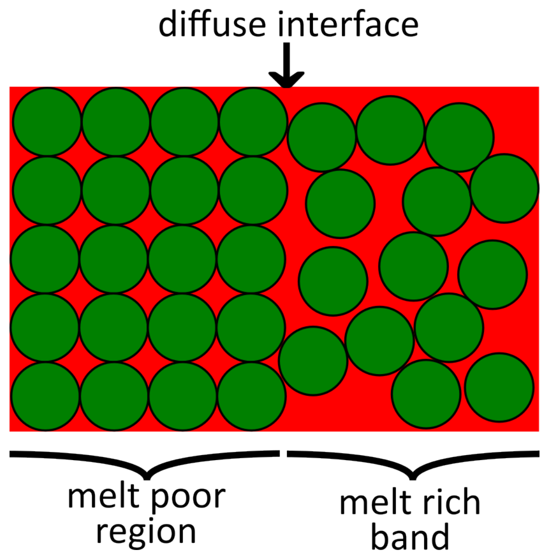


Figure 3: Cartoon showing the nature of the diffuse interface between the densely packed particles of the melt poor region and the less densely packed melt rich bands. The red is indicates melt saturated pores and the green circles are olivine grains. Inspired by Bercovici and Rudge (2016).

Bercovici and Rudge (2016) proposed that sharp melt-fraction gradients across a diffuse interface (Figure 3) act as an effective interface, generating forces similar to surface tension. This can induce a pressure term that acts like a capillary force in the narrow conduits of the granular medium, smoothing out small-scale variations in porosity and acting against the growth of high-frequency instabilities. While this explains the narrow width of melt bands seen in laboratory experiments, it struggles to define a quantitative relationship between band spacing and compaction length. They suggest that spacing may instead be controlled by a non-linear effect whereby melt is only drained from the surrounding matrix at a larger fraction of the compaction length than the band width. Alternatively, band spacing might still be governed by the homogenisation mechanism proposed by Takei and Hier-Majumder (2009), as both processes are not mutually exclusive. These factors have not been fully investigated in strain-evolving numerical models.

## 1.2 Introduction to Dilatancy and Elements of Granular Physics

In an effort to link band angles, the migration of melt in torsion experiments, and band spacing, Katz et al. (2024) took inspiration from the theory of dense granular flows. Research has well established that a solid phase can undergo net dilation relative to a surrounding fluid due to shear (Reynolds, 1885; Boyer, Buazelli and Pouliquen, 2011), introducing an additional source of stress to the system. Furthermore, Morris & Boulay (1999) predicted that suspensions of neutrally buoyant particles can radially segregate liquid and solid phases due to dilatant forces (Morris & Boulay, 1999), as seen in PMR torsion experiments (Qi et al., 2015; Qi & Kohlstedt, 2018), and Besseling et al. (2010), showed that dilatancy in dense suspensions can produce similar banding instabilities analogous to those theorised by Stevenson (1989). These studies strongly hint that dilatancy stresses could play an important role in PMR rheology.

Granular suspensions can also experience non-local fluidity (Kamrin & Koval, 2012). This is when the flow response to stress in a location is sensitive to the surrounding region, as particles need to rearrange on a grain scale to maintain geometric compatibility. Non-local fluidity is active over a region of order ten times the grain size and decreasing with the square root of shear stress, known as the cooperativity scale (Kamrin & Koval, 2012; Katz et al., 2024). Non-local fluidity could regularise band growth, creating a minimum length scale over which viscosity can vary, limiting the occurrence of high-frequency bands. This narrows the space in which melt can gather to be between the compaction length, as discussed earlier in this section, and the cooperativity scale, providing a control on band spacing.

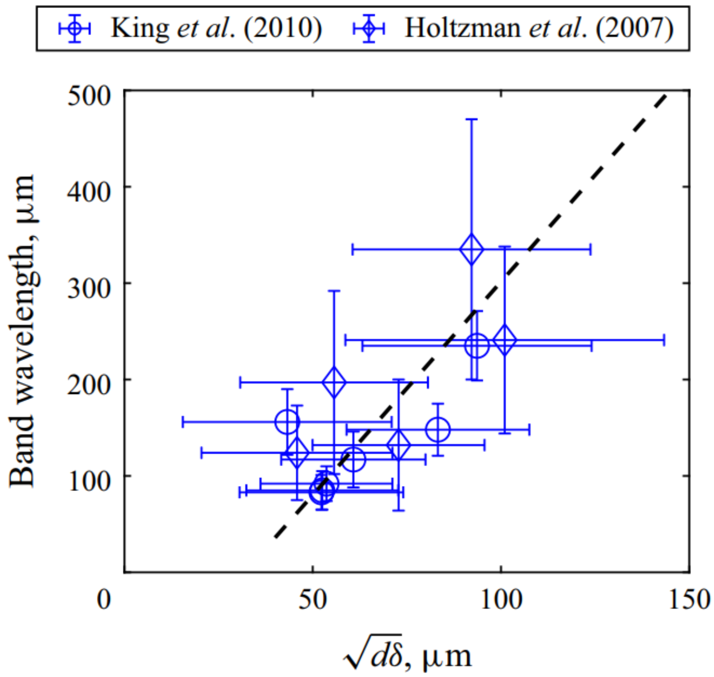


Figure 4: Wavelength of porosity bands in experiments plotted against $\sqrt{d\delta}$. The dashed line is a linear fit that respects the uncertainties in the data, suggesting a possible relationship between the cooperativity scale, non-local fluidity, and band wavelength. Taken from Katz et al. (2024).

Analytical solutions incorporating dilatancy and non-local fluidity provide good agreement with experimental studies regarding melt band angles and radial segregation (Katz et al., 2024). A linear relationship is proposed between the band wavelength, the sum of mean band spacing and mean band width, and $\sqrt{d\delta}$, where $\delta$ is the compaction length and $d$ is the mean grain size, which affects the cooperativity scale. This relationship is based on data with substantial uncertainties (Figure 4). Furthermore, grain size affects many aspects of mantle rheology, such as the diffusion length scale and capillary forces mentioned in the previous studies. Therefore, it is very difficult to pin band width and separation down to be purely an effect of non-local fluidity.

This study aims to test the theory laid out by Katz et al. (2024) and analyse the role of dilatancy in creating melt-rich bands.

## 1.3 Introduction to Dedalus

Dedalus is an open-source framework for solving partial differential equations (PDEs) using spectral methods (SMs) implemented via a Python package (Burns et al. 2020). SMs discretise variables as a finite set of basis functions, such as Fourier modes and Chebyshev polynomials (Figure 5), and solves for their coefficients in the frequency domain. This differs from what I will refer to as the 'finite' methods – finite element, finite volume, and finite difference – that discretise PDEs in space, producing a mesh of points and cells, where algebraic relationships are derived between neighboring elements to solve the PDEs. While it is possible to solve SMs in complicated geometries (Hester et al., 2021), as basis functions are set for entire coordinate directions, complexity is greatly increased. Thus, by discretising in space, 'finite' methods are much better suited for these purposes.

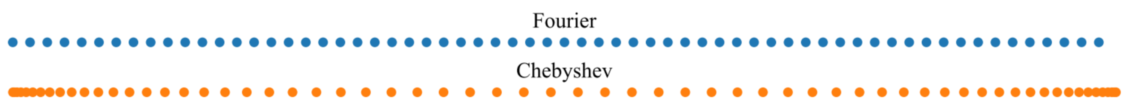


Figure 5: Example collocation grids for Fourier (blue) and Chebyshev (orange) bases in Dedalus. The Chebyshev grid clusters near the boundaries of the finite domain, while the Fourier grid is uniformly spaced and assumes periodicity (Burns et al., 2020).

The polynomials in SMs yield smooth global solutions. They are always self-consistent and cannot develop discontinuities. Furthermore, they provide exponential convergence for solutions with increasing number of modes in contrast to the polynomial convergence of 'finite' methods meaning that a greater level of accuracy can be reached with less computational power (Canuto et al., 2006). Dedalus' inbuilt methods also ensure the creation of sparse matrices for solving problems, making it particularly suitable for parallelisation and use on high-performance computing clusters (Burns et al., 2020).

SMs in Dedalus are implemented via the 'tau-method'. Additional 'tau' terms are added to the problem formulations, equivalent to the number of boundary conditions. These add extra degrees of freedom allowing the equations to be solved over polynomials exactly (Burns et al., 2020).

## 2 Methods

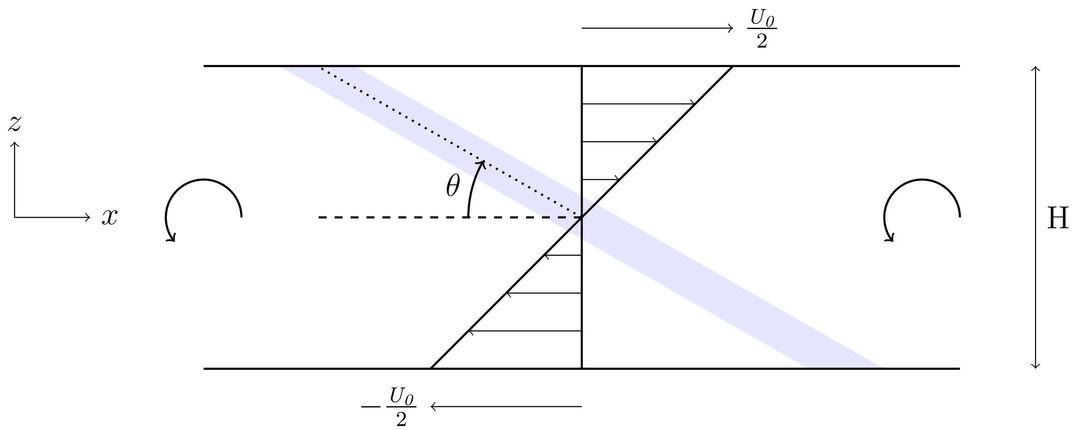


Figure 6: Simplified diagram of the problem geometry. The top and bottom surfaces are shearing. Bands (blue shading) form at angle $\theta$ from the shearing planes. The geometry is periodic in x. The height of the domain is H and the velocities at the boundaries are $(\pm U_0/2, 0)$.

Modelling PMR as interacting discrete grains and liquid networks is computationally expensive. It requires very fine meshes to resolve the small melt pockets and films dispersed in the solid matrix. Taking a representative volume element (RVE) and modelling on a continuum scale is much more efficient (Katz, 2022). The dynamics of the creeping aggregate at this scale are akin to a viscous fluid with porosity-dependent rheological laws to account for the presence of melt. Thus, motion can be described by coupling the Stokes equations for the conservation of bulk momentum (1) and mass (2) in viscous flows with Darcy's law (3), governing fluid transport through a porous medium:

$$\boldsymbol{\nabla} \cdot \bar{\boldsymbol{\sigma}} = 0, \tag{1}$$

$$\frac{\partial \bar{\rho}}{\partial t} + \boldsymbol{\nabla} \cdot \bar{\rho} \bar{\boldsymbol{v}} = 0, \tag{2}$$

$$\mathbf{q} = -\frac{k^s}{\mu^l} \boldsymbol{\nabla} P^l, \tag{3}$$

where $\bar{\boldsymbol{\sigma}}$ is the bulk stress tensor, $\bar{\rho} = \phi\rho^l + (1-\phi)\rho^s$ is the phase-averaged density, $\bar{\boldsymbol{v}} = \phi\boldsymbol{v}^l + (1-\phi)\boldsymbol{v}^s$ is the phase-averaged velocity, $\mathbf{q}$ is the segregation flux, $k^s$ is the permeability of the solid matrix, $\mu^l$ is the dynamic viscosity of the fluid, $P^l$ is the fluid pressure, and $\phi$ is the porosity. The segregation flux is volume of melt moving relative to the solid matrix and can be defined as $\mathbf{q} \equiv \phi(\boldsymbol{v}^l - \boldsymbol{v}^s)$. Thus, Darcy's law can be expressed as:

$$\phi(\boldsymbol{v}^l - \boldsymbol{v}^s) + \frac{k^s}{\mu^l}\boldsymbol{\nabla} P^l = 0. \tag{4}$$

The conservation of momentum states that the internal stresses that govern the flow are in equilibrium. The conservation of mass means that the mass can only change if there is a flux of mass in or out of a region. Darcy's law defines that the rate of fluid flow through a porous medium is a function of how easily the rock permits liquid transport, the fluidity of the liquid phase, and the pressure gradient driving the motion. It represents a momentum balance for the liquid phase relative to the solid matrix. The derivations of the coupled equations governing two-phase flows are taken from Katz (2022) unless otherwise stated.

## 2.1 Compaction Equation

The two-phase mass continuity equation is derived from the conservation of bulk mass (equation (2)). As the gravitational body forces are much weaker than the shear tractions generated by the moving plates, the Boussinesq approximation is invoked. It is assumed there is zero mass transfer between the phases, they are independently incompressible and have the same densities. The resulting equation states that the volume of material entering and leaving a region is balanced:

$$\boldsymbol{\nabla} \cdot \bar{\boldsymbol{v}} = 0. \tag{5}$$

Substituting equation (5) into the divergence of the liquid momentum balance (equation (4)) eliminates the liquid velocity and yields the following relationship:

$$-\mathcal{C} + \boldsymbol{\nabla} \cdot \left(M_\phi \boldsymbol{\nabla} P^l\right) = 0, \tag{6}$$

where $\mathcal{C} = \boldsymbol{\nabla} \cdot \boldsymbol{v}^s$ is the compaction rate of the solid grains and $M_\phi \equiv \frac{k^s}{\mu^l}$ is them mobility of the liquid phase. The equation links compaction, porosity and fluid flow stating that the divergence of the Darcy flux can drive compaction of the solid grains and vice versa.

## 2.2 Two-Phase Stokes Equation

In a two-phase system, the fluid pressure acts equally outwards in all directions. Therefore, it does not cause deformation. The bulk effective stress tensor $\bar{\boldsymbol{\sigma}}^{\text{eff}}$ describes the deformation inducing stress by removing the fluid pressure component from the bulk stress. As pressure and stress follow opposite sign conventions, the subtraction of the pressure component is achieved by its addition to the bulk stress:

$$\bar{\boldsymbol{\sigma}}^{\text{eff}} = \bar{\boldsymbol{\sigma}} + P^l \boldsymbol{I}, \tag{7}$$

where $\boldsymbol{I}$ is the identity matrix imposing equal fluid pressure in all directions. The bulk effective stress can also be expressed in terms of the isotropic strain and deviatoric strain rates:

$$\bar{\boldsymbol{\sigma}}^{\text{eff}} = \zeta_\phi \mathcal{C} \boldsymbol{I} + 2\eta_\phi \dot{\boldsymbol{\varepsilon}}, \tag{8}$$

where $\zeta_\phi$ is the compaction viscosity , $\eta_\phi$ is the shear viscosity and $\dot{\boldsymbol{\varepsilon}}$ is the deviatoric strain rate tensor:

$$\dot{\boldsymbol{\varepsilon}} = \frac{1}{2} \left[ \boldsymbol{\nabla} \boldsymbol{v}^s + (\boldsymbol{\nabla} \boldsymbol{v}^s)^T - \frac{2}{3} \mathcal{C} \boldsymbol{I} \right]. \tag{9}$$

The isotropic part ($\zeta_\phi \mathcal{C} \boldsymbol{I}$) represents the resistance of the aggregate to compaction, during which the solid matrix contracts, reducing pore space and expelling fluids. As in equation 7, $\boldsymbol{I}$ enforces equal compaction in all directions. The deviatoric part ($2\eta_\phi \dot{\boldsymbol{\varepsilon}}$) describes the aggregate's resistance to shear, a full derivation of which can be found in Katz (2022).

By substituting equation (7) into equation (8), and subsequently into the conservation of momentum (equation (1)), the two-phase Stokes equation is derived:

$$-\boldsymbol{\nabla} P^l + \boldsymbol{\nabla} \cdot 2\eta_\phi \dot{\boldsymbol{\varepsilon}} + \boldsymbol{\nabla} \zeta_\phi \mathcal{C} = 0, \tag{10}$$

dictating that pressure gradients are balanced by viscous stresses, thus describing the flow of a two-phase viscous fluid.

### 2.2.1 The Dilatancy Term

Dilatancy is added via an additional term that quantifies the normal stresses generated by grain–grain interactions (Katz et al., 2024), modifying the effective stress tensor to:

$$\bar{\boldsymbol{\sigma}}^{\text{eff}} = \zeta_\phi \mathcal{C} \boldsymbol{I} + 2\eta_\phi \dot{\boldsymbol{\varepsilon}} - D_\phi \boldsymbol{\Lambda} \dot{\varepsilon}_{II}, \tag{11}$$

where $D_\phi$ is the dilational viscosity that describes resistance to dilational deformation, $\dot{\varepsilon}_{II}$ is the second invariant of the deviatoric strain rate tensor ($\dot{\varepsilon}_{II} \equiv \sqrt{\dot{\boldsymbol{\varepsilon}} : \dot{\boldsymbol{\varepsilon}}/2}$) that records the magnitude of the distortional deformation rate, and $\boldsymbol{\Lambda}$ is the particle stress anisotropy tensor:

$$\boldsymbol{\Lambda} = \begin{pmatrix} \Lambda_{||} & 0 \\ 0 & \Lambda_{\perp} \end{pmatrix}. \tag{12}$$

$\boldsymbol{\Lambda}$ describes the normal stresses generated by a particle-laden flow. $\Lambda_{||}$ are normal stresses in the direction of flow. As the coordinate system is aligned with the simple shear, $\Lambda_{||}$ is taken to be 1. $\Lambda_{\perp}$ is the stress in the direction normal to the shear plane. By multiplying the magnitude of the deformation rate with a directional anisotropy tensor and a dilatancy viscosity, the intensity and orientation of dilatant effects can be quantified on the stress. This modifies the two-phase Stokes equation to:

$$-\nabla P^l + \nabla \cdot 2\eta_\phi \dot{\boldsymbol{\varepsilon}} + \nabla \zeta_\phi \mathcal{C} - \nabla \cdot D_\phi \boldsymbol{\Lambda} \dot{\varepsilon}_{II} = 0. \tag{13}$$

## 2.3 Porosity Evolution Equation

A modified conservation of mass equation is used to monitor the evolution of porosity, as it tracks how much material is moving in and out of a region over time. Equation (2) is split to show the evolution of the solid and liquid phases separately:

$$\frac{\partial \phi \rho^l}{\partial t} + \nabla \cdot \phi \rho^l \boldsymbol{v}^l = 0, \tag{14}$$

$$\frac{\partial (1-\phi)\rho^s}{\partial t} + \nabla \cdot (1-\phi)\rho^s \boldsymbol{v}^s = 0. \tag{15}$$

Since all velocities in the final equations are expressed in terms of the solid phase, porosity evolution is calculated using equation (15). As in the compaction equation derivation, the Boussinesq approximation is made, it is assumed that there is zero mass transfer between the phases, they are independently incompressible, and have the same densities, resulting in the following equation:

$$\frac{\partial \phi}{\partial t} + \boldsymbol{v}^s \cdot \nabla \phi - (1-\phi)\mathcal{C} = 0, \tag{16}$$

describing how the porosity changes over time due to advection and compaction.

## 2.4 Boundary conditions

$$-\mathcal{C} + \nabla \cdot M_\phi \nabla P^l = 0 \tag{17}$$

$$-\nabla P^l + \nabla \cdot 2\eta_\phi \dot{\boldsymbol{\varepsilon}} + \nabla \zeta_\phi \mathcal{C} - \nabla \cdot D_\phi \boldsymbol{\Lambda} \dot{\varepsilon}_{II} = 0 \tag{18}$$

$$\frac{\partial \phi}{\partial t} + \boldsymbol{v}^s \cdot \nabla \phi - (1-\phi)\mathcal{C} = 0 \tag{19}$$

Equations (17), (18) and (19) are solved in the geometry shown in Figure 6. No-slip and no-penetration boundary conditions are enforced on the top and bottom surfaces which are shearing at velocities $(\pm U_0/2, 0)$.

The vertical component of Darcy's Law is:

$$\left[\phi(\boldsymbol{v}^l - \boldsymbol{v}^s) = -M_\phi \boldsymbol{\nabla} P^l\right] \cdot \hat{\boldsymbol{y}}. \tag{20}$$

The velocity boundary conditions reduce the LHS to 0. Consequently, as $k^s$ and $\mu^l$ are non-zero constants, $M_\phi$ is also non-zero. Therefore, $\boldsymbol{\nabla} P \cdot \hat{\boldsymbol{y}}$ must be 0 at the boundaries.

## 2.5 Constitutive laws

To impose the two-phase rheology, porosity-dependent constitutive laws are used that are primarily derived from laboratory experiments conducted under diffusion creep dominated conditions:

$$\eta_\phi = \eta_0 e^{-\lambda(\phi-\phi_0)}, \qquad \zeta_\phi = \frac{5}{3}\eta_\phi, \qquad M_\phi = M_0\left(\frac{\phi}{\phi_0}\right)^n, \qquad D_\phi = D_0\eta_\phi.$$

The first relationship was obtained experimentally and indicates that the shear viscosity decays exponentially with an increasing total porosity. $\lambda$ is a dimensionless constant that controls how much the porosity affects the shear viscosity. It is determined to be $\sim$27 for diffusion creep regimes (Mei et al., 2002). Takei and Holtzman (2009) determined the compaction viscosity to be $\sim 5/3$ greater than the shear viscosity experimentally. $M_0$ is a reference mobility value and $n$ is the permeability exponent taken to be 3 for PMR (McKenzie, 1984; Riley & Kohlstedt, 1991; Katz, 2022). The latter is an experimentally determined constant controlling how the permeability changes with porosity. $D_0$ is the dilatancy prefactor. The requirement that entropy production remains positive for any combination of shear and isotropic deformation restricts $D_0$ to $0 \leq D_0 < 4\sqrt{5/3}$ (Katz et al., 2024). The diltancy viscosity relationship has not been experimentally determined for PMR. This constitutive law is an estimation based on observations of particle suspensions by Deboeuf et al. (2009) that show exponential weakening of particle normal stresses with liquid fraction.

## 2.6 Nondimensionalisation and Perturbations

Equations (17), (18) and (19) are subsequently nondimensionalised using the following substitutions:

$$\begin{aligned}
[\boldsymbol{v}^s] &= U_0 \rightarrow \boldsymbol{v}^s = U_0 \boldsymbol{v}', \\
[P^l] &= P_0 \rightarrow P^l = P_0 P', \\
[\mathcal{C}] &= \frac{U_0}{H} \rightarrow \mathcal{C} = \frac{U_0}{H} C', \\
[\boldsymbol{\nabla}] &= \frac{1}{H} \rightarrow \boldsymbol{\nabla} = \frac{1}{H} \boldsymbol{\nabla}',
\end{aligned}$$

where primes indicate nondimensional values. $P_0 = \eta_0 U_0/H$, $U_0$ is the velocity of the imposed shear, $H$ is the height of the domain, and $\eta_0$ is a reference shear viscosity. Parameters are scaled to these values. The primes have been omitted from this point onwards as all terms in the governing equations are nondimensional. Additionally, the superscripts have also been dropped: from here on, $\boldsymbol{v}$ will exclusively denote the solid velocity, and $P$ will exclusively denote the liquid pressure.

The porosity is decomposed into a background porosity and perturbation porosity, $\phi = \phi_0 + \phi_1$, where $\phi_0$ is set to 5%. The velocity is decomposed into a background velocity, imposed by the shearing plates, and a perturbation caused by the presence of melt, $\boldsymbol{v} = \boldsymbol{v}_0 + \boldsymbol{v}_1$. As the imposed shear is linear, $\boldsymbol{v}_0 = (y, 0) = y\hat{\boldsymbol{x}}$, resulting in the following final equations to be solved in Dedalus:

$$-\mathcal{C} + R_1 \boldsymbol{\nabla} \cdot \left(1 + \frac{\phi_1}{\phi_0}\right)^n \boldsymbol{\nabla} P = 0, \tag{21}$$

$$\boldsymbol{\nabla} P + \boldsymbol{\nabla} \cdot e^{-\lambda\phi_1}[\boldsymbol{J_2} + \boldsymbol{\nabla} \boldsymbol{v}_1 + (\boldsymbol{\nabla} \boldsymbol{v}_1)^T - \frac{2}{3}\mathcal{C}\boldsymbol{I}] + \boldsymbol{\nabla} R_2 \mathcal{C} - \boldsymbol{\nabla} \cdot D_\phi \boldsymbol{\Lambda} \dot{\varepsilon}_{II} = 0, \tag{22}$$

$$\frac{\partial \phi_1}{\partial t} + (z\hat{\boldsymbol{x}} + \boldsymbol{v}_1) \cdot \boldsymbol{\nabla} \phi_1 - (1 - \phi_1 - \phi_0)\mathcal{C} = 0, \tag{23}$$

where,

$$R_1 = \frac{M_0 \eta_0}{H^2} = \frac{\delta^2}{H^2}, \qquad R_2 = \frac{\zeta_\phi}{\eta_\phi} = \frac{5}{3}, \qquad \boldsymbol{J_2} = \begin{pmatrix} 0 & 1 \\ 1 & 0 \end{pmatrix}.$$

$\boldsymbol{J_2}$ is derived from the gradient and gradient transpose of the background velocity in the deviatoric strain rate tensor.

## 2.7 Implementing in Dedalus

The equations were solved in two main configurations: using instantaneous solvers with imposed porosity fields, and a strain-evolution model in which porosity was allowed to evolve dynamically. All models use Fourier basis functions were used along the x-axis to ensure periodicity and Chebyshev polynomials along the z-axis to enforce the boundary conditions.

### 2.7.1 Comparison to Linearised Stability Analysis

A linearised stability analysis is an established analytical solution that determines whether perturbations grow or decay. Results of the numerical model solutions are validated by comparing them to the analytical solution outlined in Katz et al. (2024). This solution obtained by deriving an equation for the irrotational and solenoidal component of the velocity field. The former is attained by eliminating the liquid pressure gradient in the compaction equation (17) using two-phase Stokes equation (18). Taking the curl of the two-phase Stokes equation (18), results in an equation governing the solenoidal velocity field. This eliminates the liquid pressure from the equations so that there is only one unknown: the solid velocity. These are coupled with the porosity evolution equation (19). Imposing a uniform background porosity field, the reference state, with an infinitesimally small sinusoidal perturbation, allows variables to be expanded to the first order, linearising the coupled equations. In the reference state the velocity gradient is equal to the strain-rate, $\dot{\gamma}$, and the compaction rate is zero. These solutions are used to solve the perturbation equations and calculate the growth rate, $\dot{s}$, resulting in the following analytical solution:

$$\dot{s} = (1-\phi_0)\frac{\lambda\dot{\gamma}}{3}\frac{(\delta k)^2}{1+(\delta k)^2}\left[\mathrm{sin}2\theta - \frac{D_0}{2}\frac{(\mathrm{sin}^2\theta + \Lambda_\perp \mathrm{cos}^2\theta)\mathrm{sin}^2 2\theta}{1-\frac{D_0}{4}(1-\Lambda_\perp)\mathrm{sin}4\theta}\right], \tag{24}$$

where $k$ is the wavenumber of the sinusoidal porosity perturbation. This solution is nondimensinalised using the following relationships:

$$\begin{aligned}
[\dot{s}] &= \frac{U_0}{H} \rightarrow \dot{s} = \frac{U_0}{H}\dot{s}', \\
[\dot{\gamma}] &= \frac{U_0}{H} \rightarrow \dot{\gamma} = \frac{U_0}{H}\dot{\gamma}', \\
[\delta] &= H \rightarrow \delta = \frac{\delta'}{H},
\end{aligned}$$

where primes indicate nondimensional values. These modifications result in the following benchmark:

$$\dot{s}' = (1-\phi_0)\frac{\lambda\dot{\gamma}'}{3}\frac{k^2}{\frac{1}{R_1'}+k^2}\left[\mathrm{sin}2\theta - \frac{D_0}{2}\frac{(\mathrm{sin}^2\theta + \Lambda_\perp \mathrm{cos}^2\theta)\mathrm{sin}^2 2\theta}{1-\frac{D_0}{4}(1-\Lambda_\perp)\mathrm{sin}4\theta}\right], \tag{25}$$

where $R_1' = (\delta'/H)^2$.

For the numerical model, a perturbation porosity field is imposed:

$$\phi_1 = A\mathrm{cos}(k_x x + k_z z), \tag{26}$$

where A is the amplitude of the porosity (A = 0.0001), $k_x = |\mathbf{K}|\mathrm{sin}\theta$, $k_z = |\mathbf{K}|\mathrm{cos}\theta$, and $|\mathbf{K}|$ is the magnitude of the wave-vector of the imposed field which is equivalent to the wavenumber $k$. $k$ is chosen to be $\sim$38 to ensure perturbations are significantly smaller than the compaction length and maximum growth rate is achieved (Katz et al,. 2024). The width of the domain is adjusted to ensure periodicity along the x-axis and that the centre of the field is always occupied by the centre of a high porosity band. Equations (21) and (22) are solved using the non-linear boundary value problem (NLBVP) solver in Dedalus for pressure and velocity. A second linear boundary value problem (LBVP) solver converts the perturbation velocity into the compaction rate. By taking the value at the centre of the field, the effect of the boundary conditions on the compaction rate are minimised and the growth rate of the bands can be calculated as:

$$\dot{s}' = \frac{\mathcal{C}'(1-\phi_0)}{A}. \tag{27}$$

The growth rate from the numerical model is calculated at 5° intervals from 0° to 180°. 180 modes are used in along the x- and z-axis (see Appendix 1 for example code).

### 2.7.2 Strain Evolution Model

The model iterates between an NLBVP and initial value problem (IVP) solver. A starting random porosity field is generated using an in-built Dedalus function. The NLBVP solves equations (21) and (22) for the pressure and perturbation velocity given a set porosity field. The IVP solves equation (23) to calculate a new porosity field, for a timestep of 0.01 given the outputs of velocity perturbation and pressure from the NLBVP. The new porosity field is subsequently fed into the first set of equations. This process is continued until a target strain of 3.1 is reached. 56 modes are used in along the x- and z-axis. An example code is included in the Appendix 2.

### 2.7.3 Poiseuille Flow

This simulation is implemented identically to the strain strain-evolution model, bar two modifications to the two-phase Stokes Equation (22). Flow at the top and bottom boundaries are set to the same velocity. This creates a linear background velocity profile, invariant in z, eliminating the $\boldsymbol{J_2}$ term. Additionally, a pressure forcing of magnitude $h$ in the x direction is introduced:

$$\boldsymbol{\nabla} P + \boldsymbol{\nabla} \cdot e^{-\lambda\phi_1}[\boldsymbol{\nabla}\boldsymbol{v}_1 + (\boldsymbol{\nabla}\boldsymbol{v}_1)^T - \frac{2}{3}\mathcal{C}\boldsymbol{I}] + \boldsymbol{\nabla} R_2\mathcal{C} - \boldsymbol{\nabla} \cdot D_\phi \boldsymbol{\Lambda}\dot{\varepsilon}_{II} = -h\hat{\boldsymbol{x}} \tag{28}$$

# 3 Results

## 3.1 Growth Rate Spectra and Linear Stability Analysis

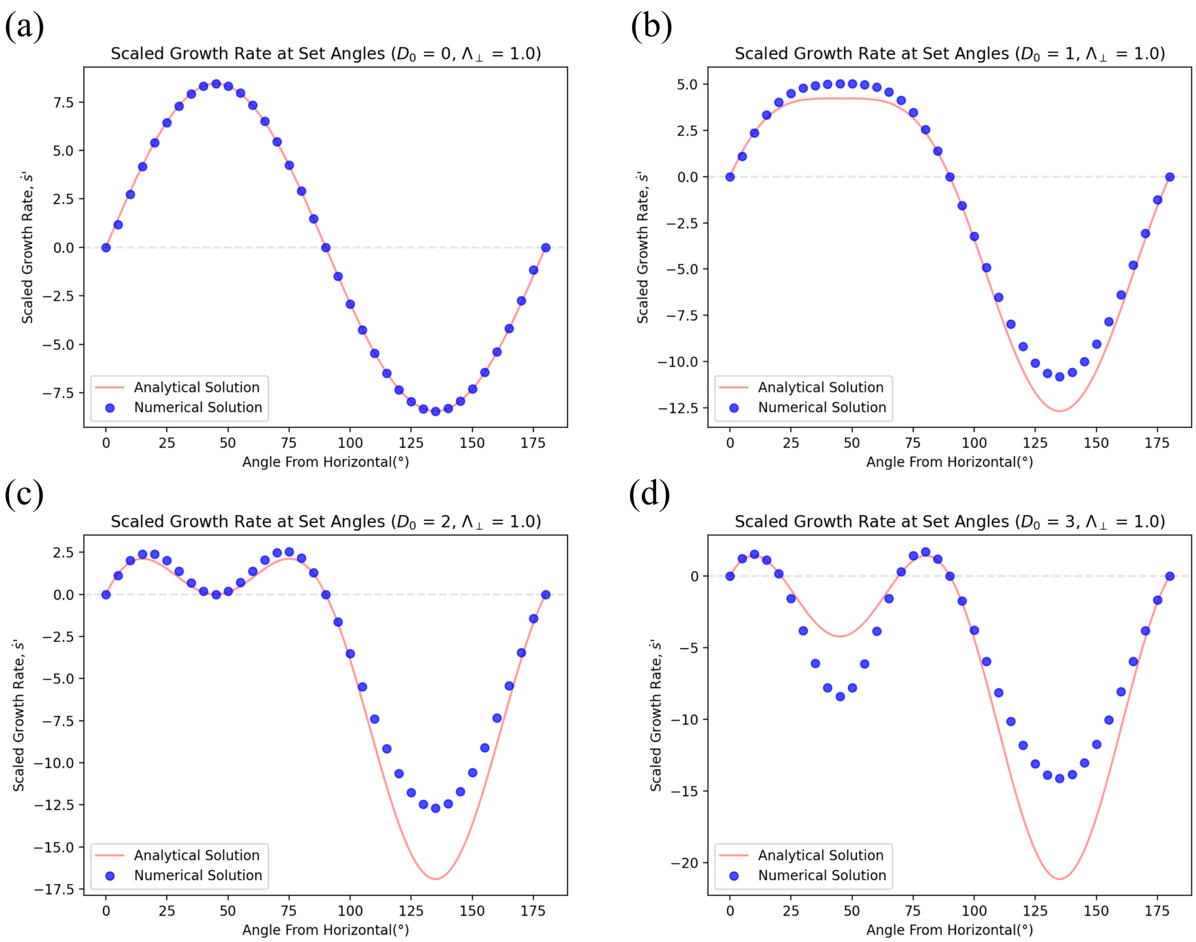


Figure 7: Comparison of the numerical model perturbation growth rates against the analytical solutions for angles 0-180°. $\Lambda_\perp$ is held at 1 and $k \sim 38$. (a) $D_0 = 0$, (b) $D_0 = 1$, (c) $D_0 = 2$, (d) $D_0 = 3$.

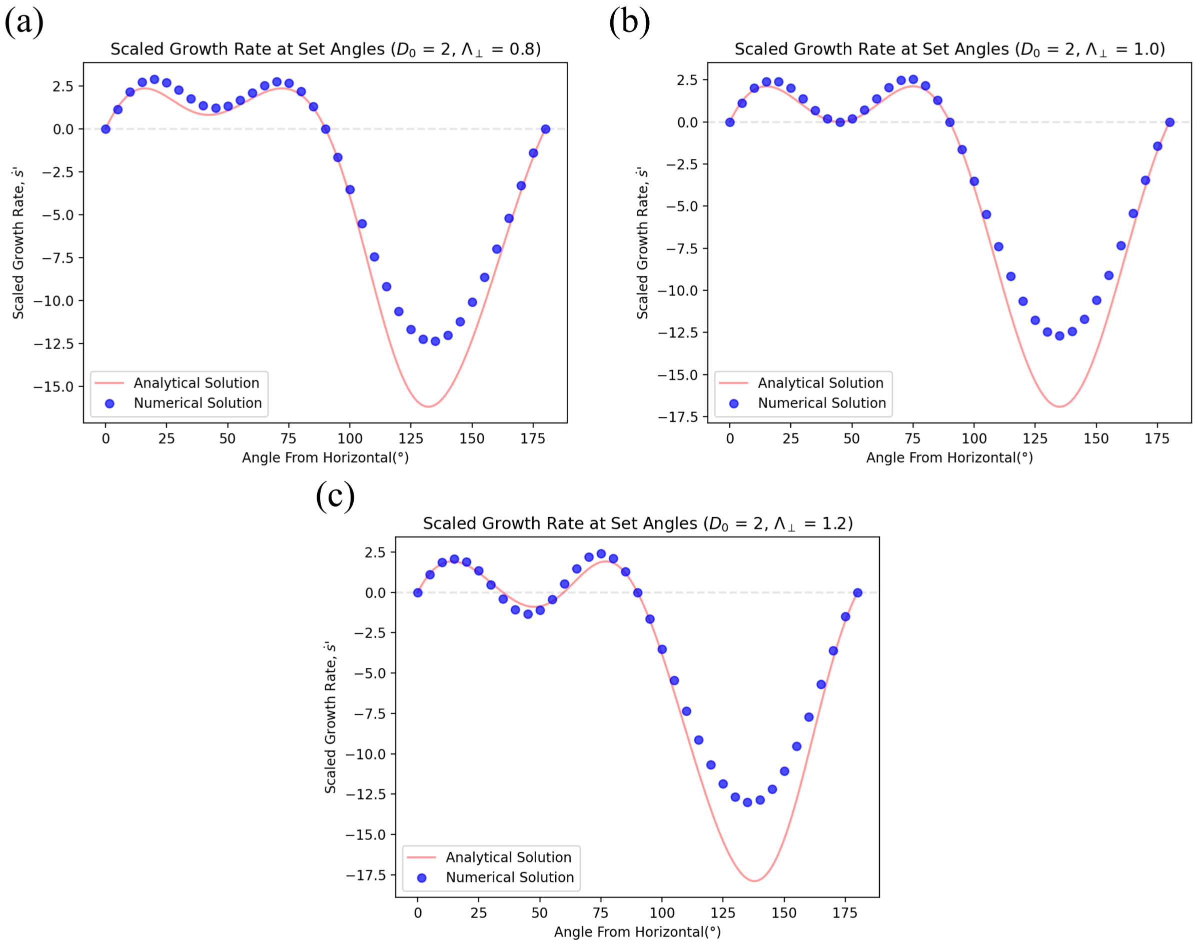


Figure 8: Comparison of the numerical model perturbation growth rates against the analytical solutions for angles 0-180°. $D_0$ is held at 2 and $k \sim 38$. (a) $\Lambda_\perp = 0.8$, (b) $\Lambda_\perp = 1.0$, (c) $\Lambda_\perp = 1.2$.

The numerical models show some agreement with the benchmarks (Figures 7 & 8). They accurately reproduce the shape of the benchmark growth spectra but fail to match the amplitude when the dilational stresses are introduced to the two-phase Stokes equation.

For $D_0 = 0$, there is no dilatancy. Band angles grow from 0-90° and decay between 90° and 180°. Peak growth rate is at 45° degrees. The growth rate curve is symmetric in amplitude, and bands emerge as quickly as they are destroyed.

The incorporation of the dilatancy term suppresses the growth rate peak and amplifies the negative growth rate. Therefore, low-angle bands develop slower, and high-angle bands are destroyed faster. At $D_0 = 1$, the growth rate has a broad peak. Thus, bands will initially grow at a broader range of angles than in the case without dilatancy. When $D_0 \geq 2$ there are two peak growth rates. For $D_0 = 2$ these are at $\sim 15 - 20°$ and $\sim 70 - 75°$. For $D_0 = 3$ the maxima are at $\sim 10 - 15°$ and $\sim 75 - 80°$. Due to the shear, bands are constantly rotated and those forming at higher angles will be rotated into the negative growth rate field. As a result, bands at lower angles are preferentially preserved.

The effects of the particle stress anisotropy tensor are much more muted than that of $D_0$. If $\Lambda_\perp < 1$ band growth is slightly accelerated growth and destruction is slowed relative to $\Lambda_\perp = 1$ . If $\Lambda_\perp > 1$, band growth is slightly suppressed and destruction is accelerated relative to $\Lambda_\perp = 1$. Increasing $\Lambda_\perp$ encourages bands to grow at slightly more extreme angles. However, these variations are practically insignificant compared to those induced by $D_0$.

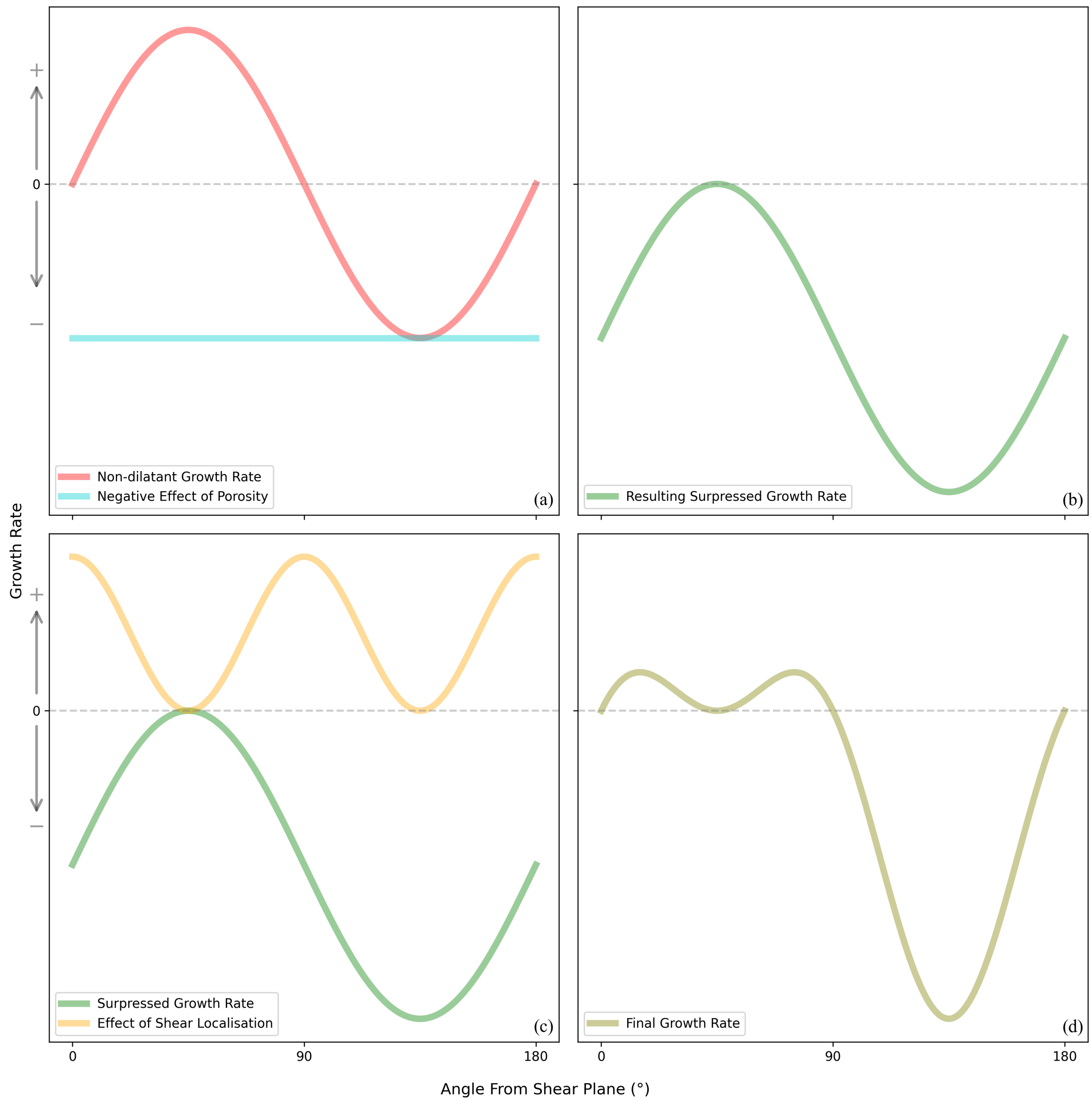


Figure 9: Diagram showing how dilatancy causes the double-peaked growth rate spectra. (a), the red line shows the growth rate of melt-rich bands when dilatant stresses are excluded from the two-phase Stokes equations. The cyan line represents the effect of increasing melt-fraction pushing grains apart, reducing their ability to interact and dilate. (b) shows the resultant curve from combining these two effects, modifying the shape of the original growth rate spectrum. (c) depicts the curve from (b) and the band angle dependent strength of dilatancy causing shear localisation, which is strongest at band orientations of 0° and 90° from the shear plane. (d) presents the overall growth rate spectrum resulting from all these interactions, with a low-angle peak growth rate, matching experiments.

The unique shape of the dilatancy growth spectra is the manifestation of two competing mechanisms found in granular two-phase flows (Katz et al., 2024). Greater melt fractions push grains apart and reduce the grain-grain interactions that result in dilatation. In the context of melt segregation, the presence of any porosity would cause the growth rate to decrease regardless of a band's orientation relative to the shear planes. The second mechanism is driven by porosity perturbations creating variations in the shear viscosity which consequently alter the rate of shear strain. As the stresses arising from dilatancy are dependent on the magnitude of the shear strain rate, porosity perturbations that are orientated favourably to dilate and localise shear strain at 0° and 90° will grow. The effect of this mechanism is proportional to $\cos^2 2\theta$. These interactions are illustrated in Figure 9.

## 3.2 Strain Evolution Models

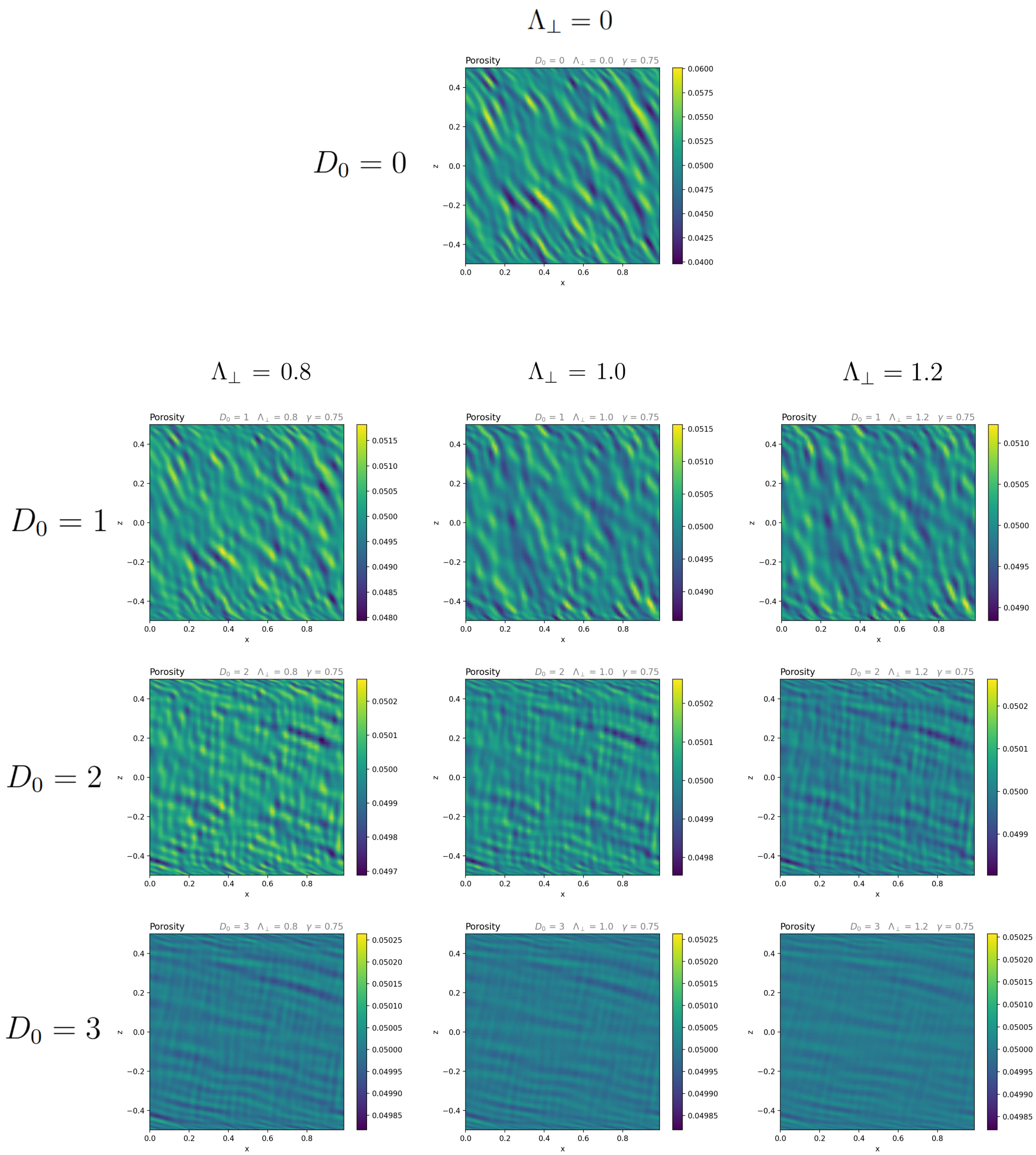


Figure 10: Grid of frames from the strain evolution models at $\gamma = 0.75$, illustrating the formation of bands. Rows lower down in the grid have higher $D_0$. Columns further to the right, have higher $\Lambda_\perp$.

All models show the development of porosity bands after enough strain has been applied (Figure 10).

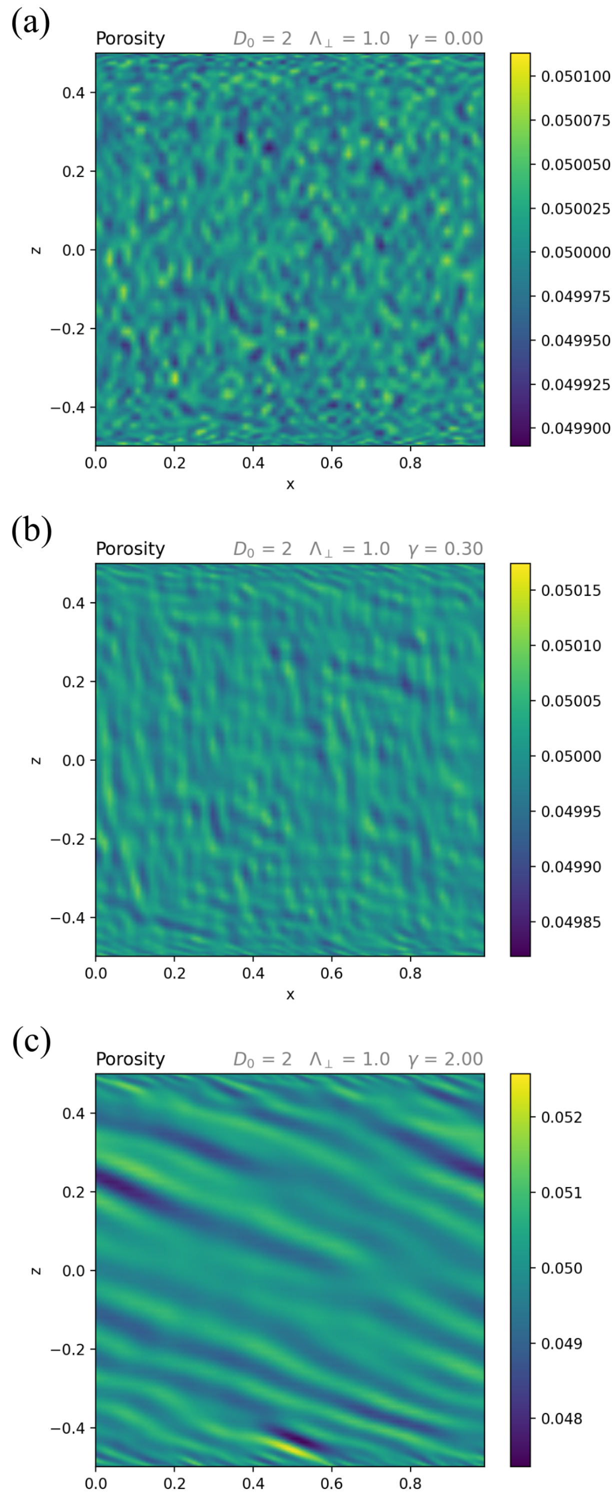


Figure 11: Frames showing porosity bands forming from a random porosity field when $D_0 = 2$ and $\Lambda_\perp = 1$. (a) starting random porosity field ($\gamma = 0.0$). (b) shallow and subvertical melt networks forming at the peak growth rate angles ($\gamma = 0.30$). (c) low-angle porosity bands, similar in orientation to experimental studies ($\gamma = 2.00$).

At the lowest strains, regions of high porosity connect to form larger networks that very quickly develop into linear structures angled at the peak growth rates (Figure 11). These structures often intersect when $D_0 \geq 2$. All networks are simultaneously advected and rotated by the induced shear. Bands increase in amplitude with as the strain grows and more melt can be segregated.

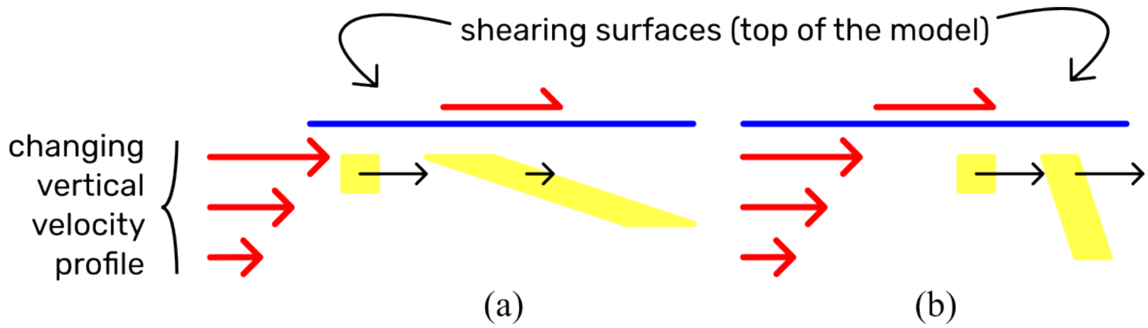


Figure 12: Diagram showing the differing effects of band angles on shear localisation and band growth. (a) low-angle bands localise shear along their structures. This slows their advection and rotation, allowing melt to advect into them. (b) subvertical bands localise shear orthogonal to their direction and have a large gradient in velocity across them. This works to advect and rotate networks with the background flow and stops melt entering the bands as they are being advected at a similar rate. Therefore, subvertical bands do not grow greatly in amplitude.

For the models run with $D_0 \geq 2$, there are two peak growth rates. The lower angled networks are strongly aligned against the direction of advection: the ends are facing the direction of the induced flow. Therefore, shear localisation due to the porosity weakening rheology acts to slow band advection. This process increases band amplitude and width. Their slow movement means that porosity perturbations can easily be advected into the ends of the bands to increase the band's amplitude (Figure 12). Higher angled networks sit almost perpendicular to the dominant flow. This maximises the vertical velocity gradient across them. Furthermore, the direction of maximum shear localisation is orthogonal to their sub-vertical structure. These factors work to advect and rotate them at a fast rate so laterally adjacent material cannot enter the bands easily. As a result, they do not grow greatly in amplitude. With increasing strains, they are rotated to angles over 90° into the negative growth field and the structures are subsequently destroyed resulting in low-angle bands dominating the field.

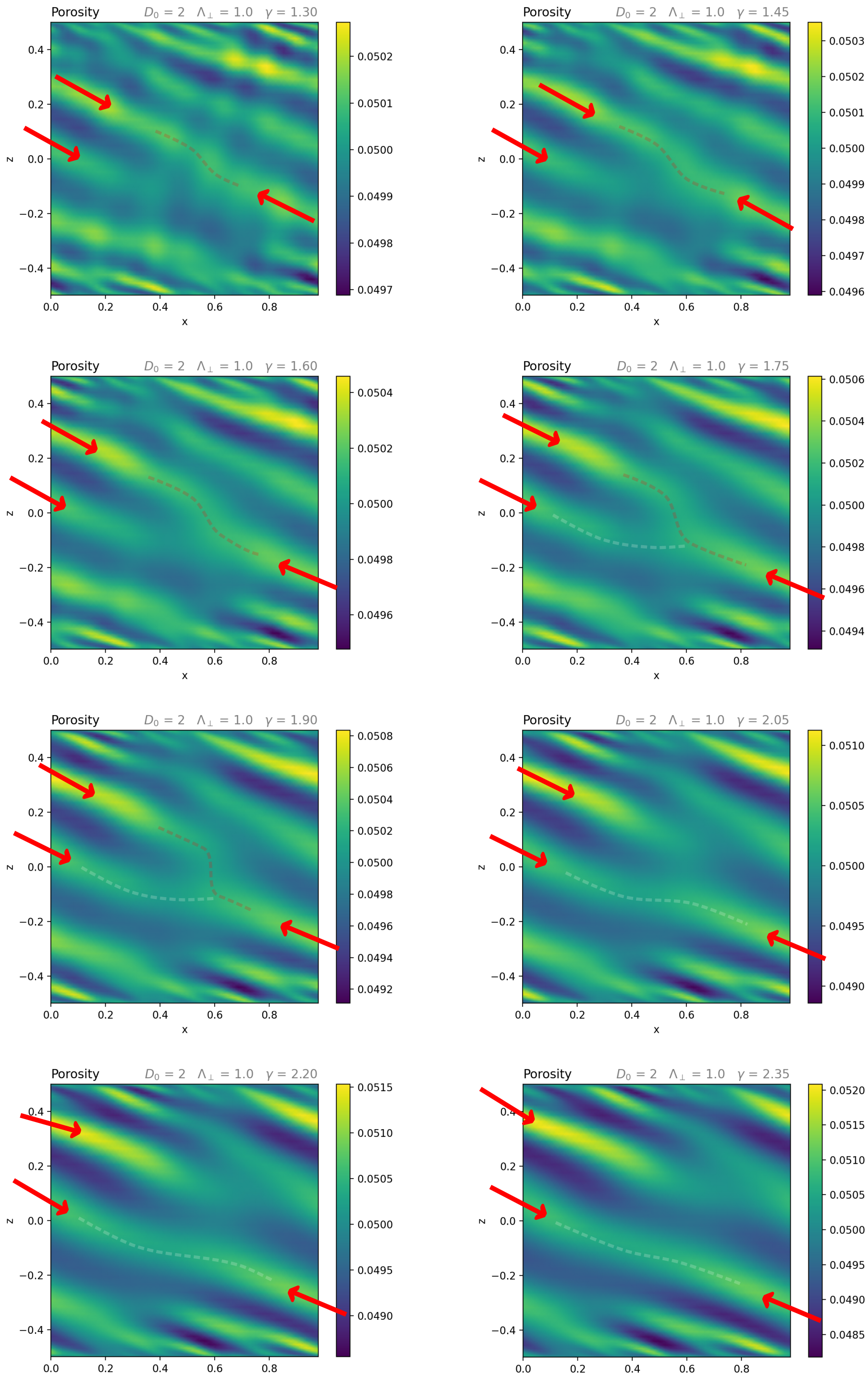


Figure 13: Frames of porosity band maintenance taken at strain intervals of $\gamma = 0.15$, beginning at $\gamma = 1.30$ and ending at $\gamma = 2.35$. Arrows indicate the bands of interest. The pale red line marks the original band as it rotates out of a favorable orientation, while the pale white line highlights a new band rotating into a more favorable position for growth.

At intermediate and higher strains, all preserved bands can be rotated enough to be at unfavorable angles and experience a negative growth rate. This often occurs in the middle of the field where the shear induced background velocity changes direction. The angle at which band destruction occurs is determined by when the growth rate crosses the x-axis into the negative field (see Figures 7 and 8). For models where $D_0 \leq 1$, $D_0 = 2$ and $D_0 = 3$, this occurs at threshold of 90°, 45/90° and ∼23° degrees, respectively. The bands split in two at their highest angle point, the threshold, and then connect with the following band being advected into its path. Between the disconnection of the old band and connection of the new band, a slightly melt enriched area develops at a shallow angle between the two band ends that will join. The shallow angle allows the porosity perturbation to grow in magnitude, acting as a 'glue' where shear can localise. It will eventually connect the bands once they have been advected far enough to be well aligned.

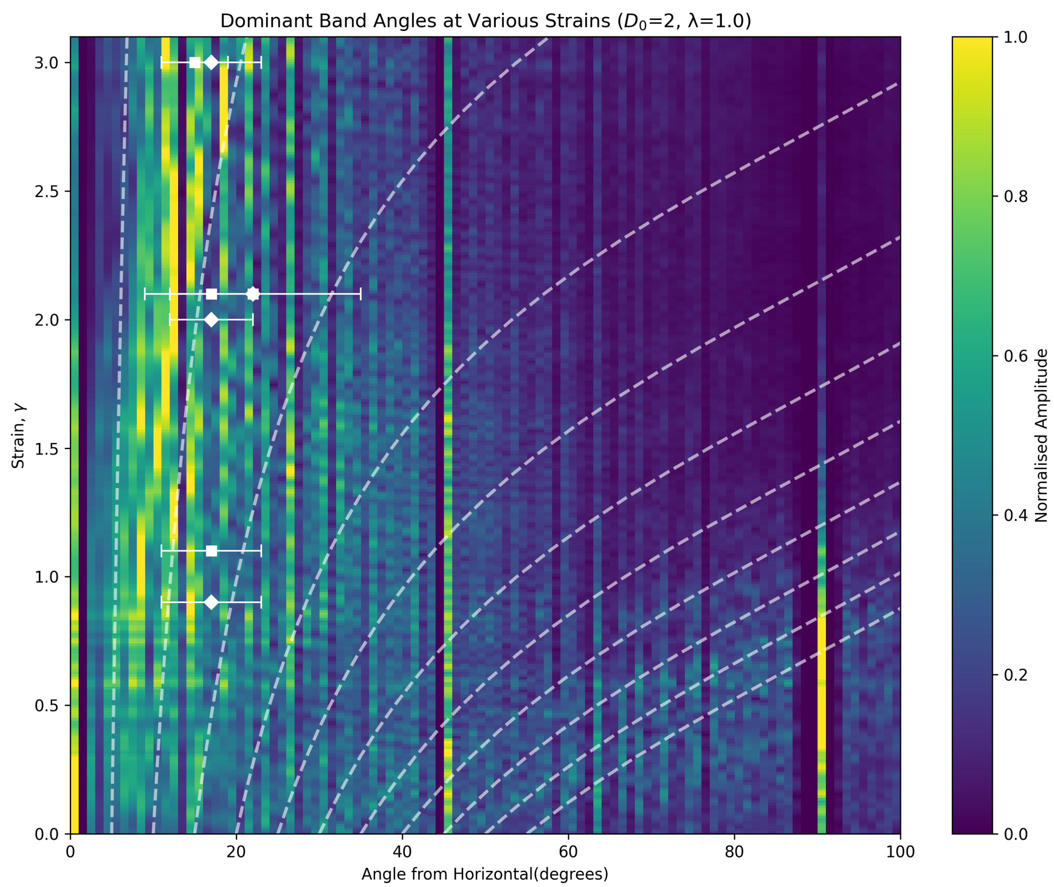


Figure 14: Spectral dataset showing how dominant band angles evolve with strain when $D_0 = 2$ and $\Lambda_\perp = 1$. The white dotted lines are the passive advection trajectories of bands from simple shear, taken from Katz (2022). The white markers are band angles calculated from PMR simple shear experiments. The squares are from Holtzman et al. (2003) and the rhombi are from Holtzman et al. (2007)

These processes can also be observed in the spectral dataset (Figure 14) that shows the dominant band angles with increasing strain. At the start of the simulations, the porosity is random and the only clearly dominant angles are at 0°, 45° and 90°, which I interpret to be a result of the grid data used to calculate the band angles. With increasing strain, angles at the peaks of the growth rate spectrum become more dominant. However, the higher peaks seem to follow the passive advection pathway until they are destroyed. The low-angle peaks dominate at greater strains. The advection of the low-angle bands is also clear. Several branches diverge off the main band angle pathway (or trunk). These seem to follow the passive advection trajectory of low-angle bands. These branches seem to be truncated at the threshold value for the model parameters (see Appendix 3 for more spectra). The experimental studies match the parameters $D_0 = 2$ and $\Lambda_\perp \approx 0.8 - 1$ the most closely.

Models become unstable when strong gradients in porosity and shear viscosity develop. This occurs earlier with lower $D_0$.

## 3.3 2D Poiseuille Flow

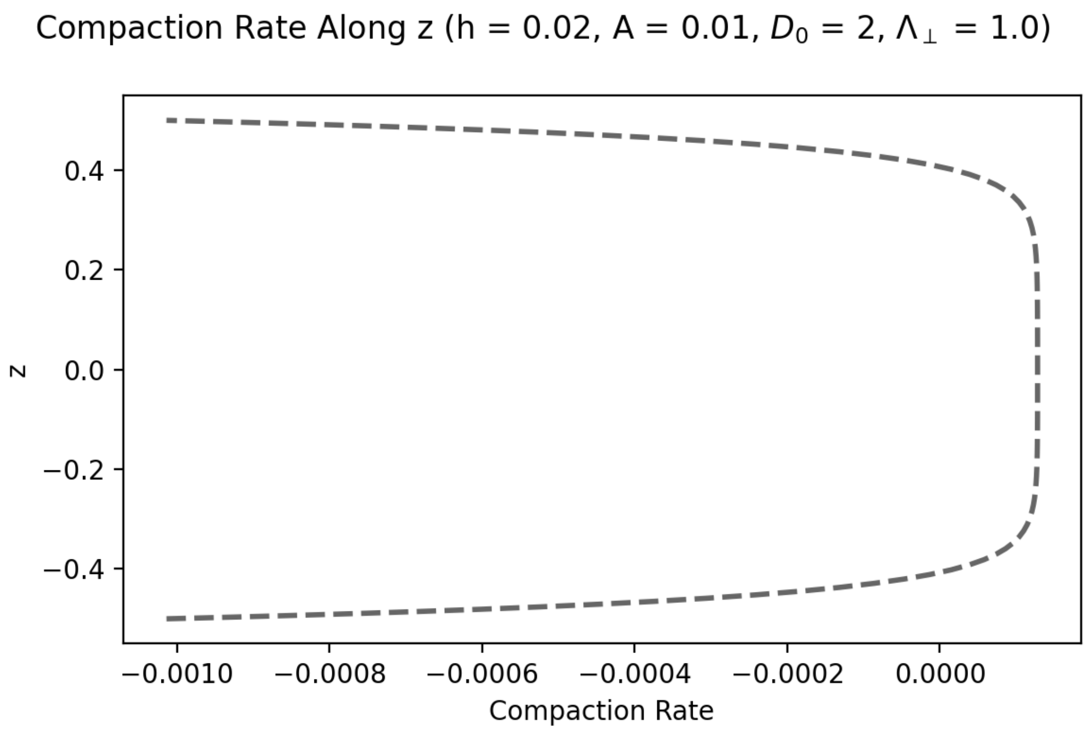


Figure 15: Compaction rate due to Poiseuille flow across a vertical melt band.

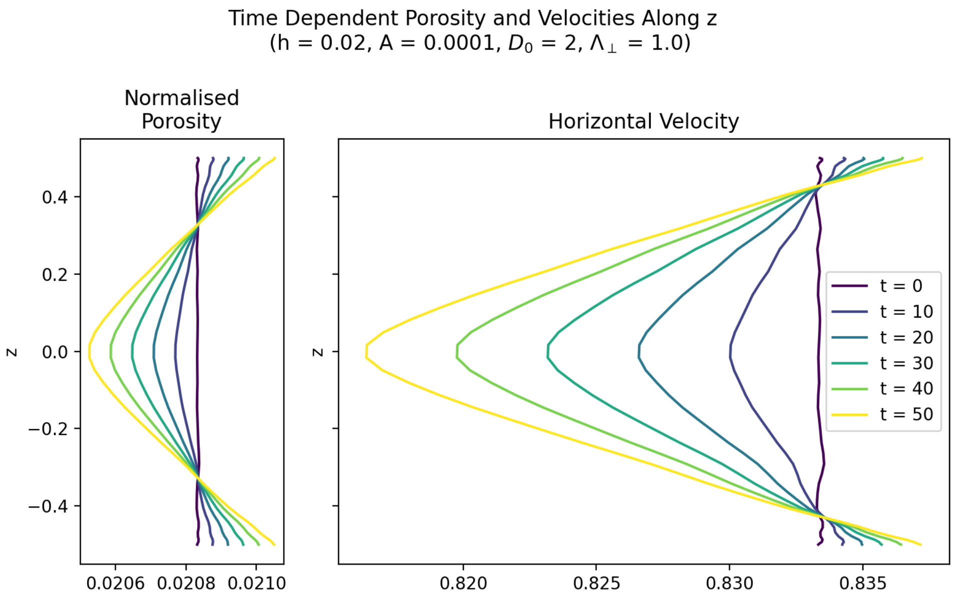


Figure 16: Plot showing the porosity being redistributed to the margins with increasing timesteps. As the overall flow is negative, the plot also shows the fastest velocities to be in the core of of the model. It is accelerating.

The models show that the compaction rate is greatest along the central axis (Figure 15), where flow velocity is the fastest, and negative at the boundaries. Thus, porosity is redistributed from areas of higher flow to slower regions: adjacent to the no-slip surfaces (Figure 16). Over time, this creates a layered structure where porosity peaks at the boundaries and is invariant in x, parallel to flow. Models with varying strengths of forcings ($h$ = 1, 0.1, 0.01, 0.001) produced similar results, albeit at different rates and with varying degrees of curvatures in velocity profiles.

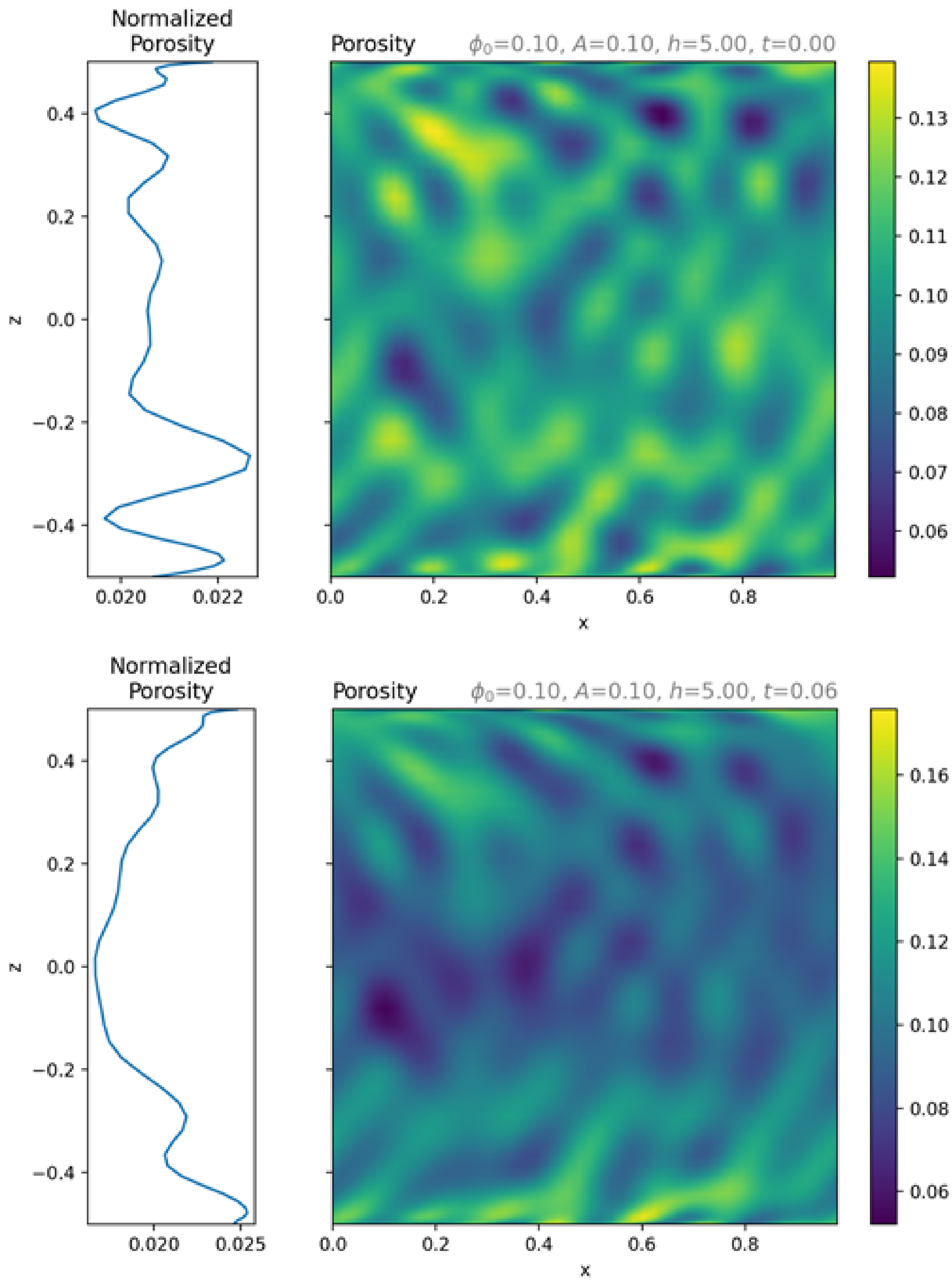


Figure 17: Plots showing the porosity being redistributed to the margins and favourably angled bands being preserved.

Increasing the amplitude of the porosity perturbation and the strength of the forcing produced a pattern with the slightest resemblance of melt bands forming (Figure 17). Favourable orientations are preserved and unfavourable orientations are slowly diminished. There is no large scale restructuring of the porosity pattern and the perturbations are primarily advected with the flow. Additional frames varying the strength of forcing and amplitude of the porosity perturbation can be found in Appendix 4.

# 4 Discussion

## 4.1 Comparisons With Experiments and Other Models

The lack of coherence in the growth rate amplitudes from the linear stability analysis may indicate that the numerical model may add additional physics that is not present in the analytical solution. One such example is the effects of the no-slip and no-penetration boundary conditions which are not included in the benchmark. They provide a hard surface that limits the flow direction, thus amplifying compaction and decompaction at the boundaries. By taking values from the centre of the field, the effect of these boundaries is minimised but may not be fully diminished. Another factor for the discrepancy could be the size of the porosity perturbation. The analytical solution assumes an infinitesimally small porosity perturbation. The perturbations used in the numerical model are greater and more representative of the samples used in experiments. However, this could result in greater shear localisation and solid decompaction, increasing the growth rate of melt bands.

The results show that when $D_0 \approx 2$ and $\Lambda_\perp \approx 0.8 - 1$, band angles most similar to those observed in experiments are formed. This is mostly in alignment with the analytical solutions set out in Katz et al. (2024), which states that the solution using $D_0 = 2$ and $\Lambda_\perp = 1$ produces growth rates that most closely resemble experiments. The effects of $\Lambda_\perp$ are very weak and insignificant in comparison to the $D_0$. Therefore, this slight discrepancy between the analytical and numerical solutions does not substantially affect the system, and the lack of consensus on constraining its value from experiments (Guazelli & Pouliquen, 2018) does not prohibit the accurate modelling of PMR if $D_0$ is known.

A major assumption of the model is that the dilatant viscosity used is true to the rheology of PMR. The relationship $D_\phi = D_0\eta_\phi$ is an estimate derived from particle suspension experiments (Debouf et al., 2009) as there have been no direct measurements of the dilation viscosity in PMR. While suspensions can sometimes behave in a way somewhat analogous to PMR, they are not fully representative of mantle rheology. Therefore, the assumption that dilatant viscosity is a simple multiple of the shear viscosity may be inaccurate. Furthermore, the tested range of $D_0$ values were narrowed down mathematically. While the resulting range of values could all be physically possible, it does not preclude the fact that the actual range in nature may be much narrower. The observation that a $D_0 = 2$ for PMR can recreate the low angle bands seen in experiments does not make it a universal rule for mantle rheology. Rather, it states that if the mantle has $D_0 \approx 2$ then dilatancy could be a dominating force in band formation. If experimental studies determine that $D_0 \approx 2$, the role of dilatancy in governing PMR rheology must be reconsidered.

The strength of dilatancy is unknown in the mantle. Therefore, it is worthwhile to question what is the minimum strength of dilatancy needed to influence melt segregation. Regions of small grain size could amplify the effect of dilatancy as they reduce the shear viscosity of PMR and localise deformation. This leads to a feedback loop where shear strain localisation further reduces grain size and weakens the region. If dilatancy is a factor of the shear viscosity, then it could accelerate the softening of the PMR by encouraging melt to flow into the area. With regards to previous models of melt segregation, dilatancy does not necessarily invalidate the two-phase damage theory developed by Rudge and Bercovici (2015). As mentioned earlier, by localising strain, it can increase the flow of grains to encourage damage and increased grain pinning, limiting grain size growth. However, these are likely to be secondary to the effect of the dilatancy, which can independently segregate melt, as shown in the models.

The dilatant strain evolution models do a poor job of replicating the characteristic band widths and spacings recorded in experiments, giving a strong indication that these might be controlled by other rheological constraints. Bands grow in width and separation with increasing strain. Their separation remains shorter than the compaction length ($\delta = 1/4$, in these models) at $\gamma = 2$. Their widths are almost equal in size to their separations, in stark contrast to the narrow bands observed by Holtzman et al. (2003) that were an order of magnitude narrower than the melt-poor regions. This could be because there is no mechanism in the model to discourage short-wavelength perturbations. Granular dilatancy can act in unison with all the theories proposed to provide a lower limit for band separation: capillary effects on a diffuse interface (Bercovici & Rudge, 2016); surface tension-driven dissolution/precipitation (Takei & Hier-Hajumder, 2009; King et al., 2011); and non-local fluidity (Katz et al., 2024). Therefore, no clear conclusions can be drawn as to whether one dominates. Incorporating them into strain-evolving dilatant numerical models could help to distinguish between more reasonable hypotheses.

## 4.2 Bands and Melt extraction in the Mantle

The primary motivation for studying melt segregation is to understand how melt is concentrated and extracted at spreading centres. Seismic anisotropy beneath divergent plate margins, concentrated beneath surface expressions of magmatism, is strong evidence for sheets of melt extending for hundreds of kilometres parallel to the Ethiopian Rift (Kendall et al., 2005) and Reykjanes Peninsula (Pilidou et al., 2005). Vertical dunite sheets have also been studied in the Oman Ophiolite (Braun & Kelemen, 2002) and Trinity Peridotites, Northern California (Quick, 1982). These sheets are believed to form where the strain rates are highest: vertically near the center of rifting and at an angle where the lithosphere-asthenosphere boundary (LAB) is inclined (Rees Jones et al., 2021). Modelling has suggested that vertical melt segregation is strongly assisted by buoyancy driven reactive melt flows that dissolve the host rock, resulting in vertical networks dominating transport in the centre of the ridge at shallow depths (Rees Jones et al., 2021). Angled sheets due to shear are predicted to occur at greater depths, nearer to the LAB margins. In these regions, sheets are influenced by the passive flow of the mantle as well as the vertical gradient in shear induced by plates, leading to the emergence of networks dipping more steeply from horizontal than laboratory experiments (Katz et al., 2006). These are far harder to uplift and preserve so there is less concrete evidence for them. It is likely that melt bands influenced by dilatancy could be important for focussing melt at depth, creating lenses on the order of hundreds of metres in length (Holtzman et al., 2003), and not play an important role for shallow processes.

## 4.3 Bands and Magmatic intrusions

Magmatic intrusions, such as dykes and sills, are driven by pressure gradients. As material is caught in the rough surface of the rock margins, flow is inhibited relative to the intrusion core and shear is induced. If the rheology of PMR in intrusions is similar to that of the experiments reviewed in the introduction simulating mantle conditions, it is reasonable to hypothesise that dilatancy may contribute to the formation of melt-rich bands in intrusions, such as those examined by Nicholas (1986) and discussed in the introduction.

The Poiseuille flow example acts as a simplified analogue, recreating some of the the conditions of an in intruding flow, but neglecting the effects of cooling from colder country rock margins. Given these assumptions and simplifications, the model is not universally applicable. It is only valid under specific conditions where the rate of cooling is much slower than the rate of intrusion, and where the melt fraction of the PMR is low enough to allow strong grain-grain interactions and the applicability of mantle-like rheological laws. Thus, the model is most likely to be representative of dykes and sills near the base of the crust, where the rock's chemistry, pressure, and temperature more closely resemble those used in experimental studies, and where temperature contrasts at the margins may be more subtle.

For models using a small porosity perturbation, the primary observation of decompaction at the margins is the effect of dilatancy. As shear is greater near the no-slip boundaries, the magnitude of the distortional deformation rate, (recorded by $\dot{\varepsilon}_{II}$) also increases, amplifying the effect of dilatancy. This increases the melt fraction at the edges and pushes the solids towards the centre of the flow where the vertical velocity gradient is more shallow and the effects of dilatancy are muted. Similar behaviour was theorised by Bagnold (1954) for neutrally buoyant particles suspended in a Newtonian fluid. Related concepts have also been applied to the crystallisation of ultramafic intrusions (Bhattacharji & Smith, 1964; Simkin, 1967). However, these studies did not explicitly relate such phenomena to dilatancy in dense, granular flows.

This melt segregation could theoretically lead to the enrichment of incompatible elements, that preferentially partition into the liquid phase, nearer to the intrusion margins in addition to a slightly more evolved mineral composition. Geochemical studies of deeply intruded dykes and sills have yielded results that align with this hypothesis (Brouxel, 1991; Tarney & Weaver, 1987; Nkono et al., 2006; Latypov, 2003)(see Appendix 5 for example geochemcial data). However, shallowly intruded dykes do not show such behaviour (Namur & Humphrys, 2018; Mollo et al., 2011; Ross, 1986). This may be due to the steeper temperature gradients experienced by shallow and volcanic intrusions compared to deep crustal dykes and sills, which can cause the margins to crystallise before the melt has a chance to fully segregate to them. Therefore, intrusion transect chemistry is determined by a balance between inertial forces and cooling rate. As a result, intrusion depth is likely to be the primary controlling factor in melt distribution. However, local variables that may affect PMR velocity could create anomalies where fast moving shallow intrusions segregate melt to the margins or a very slow moving intrusion at depth cools before melt segregation.

The lack of porosity band emergence could be the result of the low strain-rates which favour the migration of melts towards the margins in the model over band creation. This is because it is not reliant on connecting and amplifying small porosity perturbations into larger bands. Furthermore, increasing the melt fractions at the margins reduces the strength of the PMR. Therefore, flow can accelerate, amplifying the efficiency of melt segregation away from the core and destroying porosity perturbations that create bands.

Increasing the size of the porosity perturbation relative to the background porosity results in greater gradients in shear viscosity in the random porosity field. This weakens the PMR, encourages strain localisation and melt band formation. However, as discussed in the results section, this system does not create straight low angled bands as the simple shear model. It preserves bands at favorable angles while slightly diminishing those at unfavorable ones.

The relatively narrow window of conditions required to form distinct melt bands in magmatic intrusions is likely to limit their occurrence in nature. However, several intrusions at mid- and low-crustal levels contain low-angle lenses enriched in minerals crystallised from more differentiated melts (Floess et al., 2019; Zavela et al., 2011, Nicolas, 1986; Nicolas and Jackson, 1982; MacLeod & Yaouancq, 2000; Puffer & Horter, 1993). The results of this study are not comprehensive enough to provide an in depth reasoning for why these show melt lenses. However, it could be suggested that their sources may have undergone heterogeneous melting causing large variations in the porosity and shear viscosity.

## 4.4 Suitability of Dedalus for Geodynamics

As Dedalus is not restricted by spatial discretisations, it can produce very accurate results using significantly fewer modes/elements than 'finite' methods require. This drastically reduces the computational cost of running models. While a greater number of modes could have been used for the strain evolution models, the increase in accuracy would have been exponentially less distinguishable and required much greater computational power. Furthermore, it is reasonably good at handling non-linear equations if they include enough linear terms to balance the non-linear terms. However, it is very difficult to quantify how non-linear equations could be and keep the problems well conditioned. Dedalus cannot solve fully non-linear equations.

The research highlighted that Dedalus has trouble dealing with sharp spatial contrasts in viscosity. This could be because it creates a quasi-discontinuity in the material properties that are hard to resolve with global basis functions. The issue arose often when using the random field generator for the porosity. When using more modes, the gradients in porosity became greater, creating sharp viscosity contrasts. This could be overcome by smoothing the initial random porosity field. However, this comes at a cost of not being able to resolve smaller melt bands.

With these considerations in mind, Dedalus could be a very powerful tool for solving non-linear equations that govern flow in the outer core, as the solutions are guaranteed to be smooth and sharp contrasts in material properties will not occur.

# 5 Conclusion

The analytical solutions of the two-phase flow equations incorporating dilatancy and non-local fluidity in Katz et al. (2024) have provided the most comprehensive analytical reasoning for melt segregation as of yet in both planar, and toroidal shear. By creating a strain evolving models, this study has tested whether the analytical model can reproduce the observations seen in experiments and magmatic intrusions. It was found that the dimensionless values of $D_0 \approx 2$ and $\Lambda_\perp \approx 0.8 - 1$ could reproduce the $\sim$15-20° band angles seen in experiments, even with the exclusion the non-local fluidity parameter. These values are consistent with our current understanding of PMR rheology. However, the signature narrow melt bands, and wide melt-poor regions could not be recreated by dilatancy alone.

The dilatant two-phase flow equations were also implemented to recreate the dynamics of igneous intrusions. The Poiseuille flow example, aimed to be analogous to a dyke or sill intruding at a rate far greater than it's cooling showed that melt can be concentrated near the margins. This aligned with geochemical studies of deeply intruded dykes.

These findings show that while the inclusion of dilatancy has improved our understanding of melt band formation, there are still many questions needing to be answered, especially regarding band width and separation. Furthermore, to understand how such phenomena can create more efficient pathways for melt extraction at mid-ocean ridges, it is essential that we gain a greater insight into grain size growth and decay in PMR as these can greatly impact the controlling factors of band formation.

Dedalus is a powerful tool for geodynamics in simple geometries. While one of its greatest strengths is self-consistency from smooth-global functions, it should be noted that it cannot resolve sharp boundaries limiting its use for studying phenomena such as dyke propagation into rock. Furthermore, its inability to solve for sharp viscosity contrasts further stably limits its applicability for some geodynamics questions.

# 6 Acknowledgments

I would like to thank my primary supervisor, Professor Richard Katz, for his patient guidance throughout this project, and my secondary supervisor, Dr Yuan Li, for his ongoing technical support. I also wish to extend my appreciation to Zhengxuan Li for his valuable advice on extracting data from my models, as well as keeping me entertained while my code was running. I am grateful to the Dedalus development team for building the Python package I have been using and creating a strong online community that has promptly replied to my debugging queries. Finally, I would like to thank the wider FoaLab research group for being a supportive community and inspiring me to connect my research to real-world observations.

# 7 Bibliography

Beeman, M.L. & Kohlstedt, D.L., 1993. Deformation of fine-grained aggregates of olivine plus melt at high temperatures and pressures, *Journal of Geophysical Research*, 98 (B4), pp. 6443-6452.

Bercovici, D. & Rudge, J.F., 2016, A mechanism for mode selection in melt band instabilities, *Earth and Planetary Science Letters*, 433, pp. 139-145.

Besseling, R., Isa, L., Ballesta, P., Petekidis, G., Cates, M.E. & Poon, W.C.K., 2010, Shear Banding and Flow-Concentration Coupling in Colloidal Glasses, *Physical Review Letters*, 105(26), pp. 268301.

Bhattacharji, s. & Smith, C. H. , 1964, Flowage Differentiation, *Science145*, 145(3628), pp. 150-153.

Boyer, F., Guazzelli, É & Pouliquen, O., 2011, Unifying Suspension and Granular Rheology, *Physical Review Letters*, 107(18), pp. 188301.

Braun, M.G. & Kelemen, P.B., 2002, Dunite distribution in the Oman Ophiolite: Implications for melt flux through porous dunite conduits, *Geochemistry, Geophysics, Geosystems*, 3(11), pp. 1–21.

Brouxel, M., 1991, Geochemical consequences of flow differentiation in a multiple injection dike (Trinity ophiolite, N. California), *Lithos*, 26(3), pp. 245–252.

Burns, K.J., Vasil, G.M., Oishi, J.S., Lecoanet, D. & Brown, B.P., 2020, Dedalus: A flexible framework for numerical simulations with spectral methods, *Physical Review Research*, 2(2), pp. 023068.

Canuto, C., Hussaini, M.Y., Quarteroni, A. and Zang, T.A., 2006. *Spectral methods*, (Vol. 285). Berlin: springer.

Chistyakova, S. & Latypov, R., 2012, Magma differentiation and crystallization in basaltic conduits by two competing petrogenetic processes, *Lithos*, 148, pp. 142–161.

Deboeuf, A., Gauthier, G., Martin, J., Yurkovetsky, Y. & Morris, J.F., 2009, Particle Pressure in a Sheared Suspension: A Bridge from Osmosis to Granular Dilatancy, *Physical Review Letters*, 102(10), pp. 108301.

Floess, D., Caricchi, L., Simpson, G. & Wallis, S.R., 2019, Melt segregation and the architecture of magmatic reservoirs: insights from the Muroto sill (Japan), *Contributions to Mineralogy and Petrology*, 174(27), pp. 1-15.

Guazzelli, É & Pouliquen, O., 2018, Rheology of dense granular suspensions, *Journal of Fluid Mechanics*, 852, pp. P1.

Hester, E.W., Vasil, G.M. & Burns, K.J., 2021, Improving accuracy of volume penalised fluid-solid interactions, *Journal of Computational Physics*, 430, pp. 110043.

Hofmann, A.W., 1988, Chemical differentiation of the Earth: the relationship between mantle, continental crust, and oceanic crust, *Earth and Planetary Science Letters*, 90(3), pp. 297–314.

Holtzman, B.K., Groebner, N.J., Zimmerman, M.E., Ginsberg, S.B. & Kohlstedt, D.L., 2003, Stress-driven melt segregation in partially molten rocks, *Geochemistry, Geophysics, Geosystems*, 4(5).

Katz, R.F., 2022, The Dynamics of Partially Molten Rock, Princeton University Press.

Katz, R.F., Rudge, J.F. & Hansen, L.N., 2024, Granular dilatancy and non-local fluidity of partially molten rock, *Journal of Fluid Mechanics*, 978, pp. A7.

Katz, R.F., Spiegelman, M. & Holtzman, B., 2006, The dynamics of melt and shear localization in partially molten aggregates, *Nature*, 442(7103), pp. 676-679.

Kendall, J.-M., Stuart, G.W., Ebinger, C.J., Bastow, I.D. & Keir, D., 2005, Magma-assisted rifting in Ethiopia, *Nature*, 433(7022), pp. 146–148.

King, D.S.H., Hier-Majumder, S. & Kohlstedt, D.L., 2011, An experimental study of the effects of surface tension in homogenizing perturbations in melt fraction, *Earth and Plane-*

*tary Science Letters*, 307(3-4), pp. 349–360.

Latypov, R.M., 2003, The Origin of Marginal Compositional Reversals in Basic–Ultrabasic Sills and Layered Intrusions by Soret Fractionation, *Journal of Petrology*, 44(9), pp. 1579–1618.

MacLeod, C.J. & Yaouancq, G., 2000, A fossil melt lens in the Oman ophiolite: Implications for magma chamber processes at fast spreading ridges, *Earth and Planetary Science Letters*, 176(3-4), pp. 357–373.

McKenzie, D., 1984. The generation and compaction of partially molten rock. *Journal of Petrology*, 25(3), pp.713-765.

Mei, S., Bai, W., Hiraga, T. & Kohlstedt, D.L., 2002, Influence of melt on the creep behavior of olivine–basalt aggregates under hydrous conditions, *Earth and Planetary Science Letters*, 201(3), pp. 491–507.

Mollo, S., Lanzafame, G., Masotta, M., Iezzi, G., Ferlito, C. & Scarlato, P., 2011, Cooling history of a dike as revealed by mineral chemistry: A case study from Mt. Etna volcano, *Chemical Geology*, 288(1-2), pp. 39–52.

Morris, J.F. & Boulay, F., 1999, Curvilinear flows of noncolloidal suspensions: The role of normal stresses, *Journal of Rheology*, 43(5), pp. 1213–1237.

Namur, O. & Humphreys, M.C.S., 2018, Trace Element Constraints on the Differentiation and Crystal Mush Solidification in the Skaergaard Intrusion, Greenland, *Journal of Petrology*, 59(3), pp. 387–418.

Nicolas, A., 1986, A Melt Extraction Model Based on Structural Studies in Mantle Peridotites, *Journal of Petrology*, 27(4), pp. 999–1022.

Nicolas, A. & Jackson, M., 1982, High Temperature Dikes in Peridotites: Origin by Hydraulic Fracturing, *Journal of Petrology*, 23(4), pp. 568–582.

Nkono, C., Féménias, O., Diot, H., Berza, T. & Demaiffe, D., 2006, Flowage differentiation in an andesitic dyke of the Motru Dyke Swarm (Southern Carpathians, Romania) inferred from AMS, CSD and geochemistry, *Journal of Volcanology and Geothermal Research*, 154(3), pp. 201–221.

Parsons, R.A., Nimmo, F., Hustoft, J.W., Holtzman, B.K. & Kohlstedt, D.L., 2008, An experimental and numerical study of surface tension-driven melt flow, *Earth and Planetary Science Letters*, 267(3), pp. 548–557.

Pilidou, S., Priestley, K., Debayle, E. & Gudmundsson, Ó., 2005, Rayleigh wave tomography in the North Atlantic: high resolution images of the Iceland, Azores and Eifel mantle plumes, *Lithos*, 79(3), pp. 453–474.

Puffer, J.H. & Horter, D.L., 1993, Origin of pegmatitic segregation veins within flood basalts, *Geological Society of America Bulletin*, 105(6), pp.738-748.

Qi, C. and Kohlstedt, D.L., 2018. Influence of compaction length on radial melt segregation in torsionally deformed partially molten rocks, *Geochemistry, Geophysics, Geosystems*, 19(11), pp.4400–4419.

Qi, C., Kohlstedt, D.L., Katz, R.F. & Takei, Y., 2015, Experimental test of the viscous anisotropy hypothesis for partially molten rocks, *Proceedings of the National Academy of Sciences*, 112(41), pp. 12616.

Quick, J.E., 1982, The origin and significance of large, tabular dunite bodies in the Trinity peridotite, northern California, *Contributions to Mineralogy and Petrology*, 78(4), pp. 413–422.

Rees Jones, D.W., Zhang, H. & Katz, R.F., 2021, Magmatic channelization by reactive and shear-driven instabilities at mid-ocean ridges: a combined analysis, *Geophysical Journal International*, 226(1), pp. 582–609.

Reynolds, O., 1885, On the Dilatancy of Media composed of Rigid Paricles in Contact. With Experimental Illustrations, *The London, Edinburgh, and Dublin Philosophical Magazine and Journal of Science*, 20(127), pp.469-481.

Riley, G.N. & Kohlstedt, D.L., 1991, Kinetics of melt migration in upper mantle-type rocks, *Earth and Planetary Science Letters*, 105(4), pp. 500–521.

Ross, M.E., 1986, Flow differentiation, phenocryst alignment, and compositional trends within a dolerite dike at Rockport, Massachusetts, *GSA Bulletin*, 97(2), pp. 232–240.

Rudge, J.F. & Bercovici, D., 2015, Melt-band instabilities with two-phase damage, *Geophysical Journal International*, 201(2), pp. 640.

Simkin, T., 1967, Flow differentiation in the picritic sills of north Skye. In: Wyllie, P. J. (ed.) Ultramafic and Related Rocks. New York: Wiley, pp. 64-69.

Spiegelman, M. & Kenyon, P., 1992, The requirements for chemical disequilibrium during magma migration, *Earth and Planetary Science Letters*, 109(3), pp. 611–620.

Stevenson, D.J., 1989, Spontaneous small-scale melt segregation in partial melts undergoing deformation, *Geophysical Research Letters*, 16(9), pp. 1067.

Takei, Y. & Hier-Majumder, S., 2009, A generalized formulation of interfacial tension driven fluid migration with dissolution/precipitation, *Earth and Planetary Science Letters*, 288(1), pp. 138–148.

Takei, Y. & Holtzman, B.K., 2009, Viscous constitutive relations of solid-liquid composites in terms of grain boundary contiguity: 2. Compositional model for small melt fractions, *Journal of Geophysical Research: Solid Earth*, 114(B6).

Takei, Y. & Katz, R.F., 2013, Consequences of viscous anisotropy in a deforming, two-phase aggregate. Part 1. Governing equations and linearized analysis, *Journal of Fluid Mechanics*, 734, pp. 424-455.

Tarney J. & Weaver, B.L., 1987, Mineralogy, petrology and geochemistry of the Scourie dykes: petrogenesis and crystallization processes in dykes intruded at depth, *Geological Society, London, Special Publications*, 27(1), pp. 217–233.

Zavala, K., Leitch, A.M. & Fisher, G.W., 2011, Silicic Segregations of the Ferrar Dolerite Sills, Antarctica, *Journal of Petrology*, 52(10), pp. 1927–1964.

# 8 Appendices

## 8.1 Example Code for Linear Stability Analysis

```
"""
Code to benchmark shearing of two-phase dilatant partially molten rock.
"""


import numpy as np
import h5py
import dedalus.public as d3
import matplotlib.pyplot as plt


eta0 = 1 # Reference shear viscosity
Lam = 27 # Porosity dependent shear viscosity exponent
bgpor = 0.05 # Background porosity
n = 3 # Permeability Exponent
A = 0.0001 # Amplitude of perturbation
H = 1  # Reference height of domain
compleng = H/4 # Compaction length
D0 = 2 # Dilatancy Prefactor
lamper = 0.8 #Perpendicular Particle Stress Anisotropy
j = 6 # Variable to set wavenumber (note that j is not the wavenumber )
num = 2 # Sets number of bands in field, 2 ensure centre is always porosity maximum
noang = 37 # Number of times growth rate is calculated between 0 and 180 degrees


angleangle = np.zeros(noang) # Array for plotting angle
s_calc = np.zeros(noang)  # Array for plotting growth rate
```

```
c_cent = np.zeros(noang) # Array for Divergence at central point (middle of a band)

for i in range(0, noang):
    #Make wave-vector to create porosity field
    angledeg = 5*i
    # Calculate growth rate for angles at every 5 degrees between 0 and 180
    angle = (angledeg)*(np.pi/180) # Convert angle to radians

    l = H / j #
    kmag =  (2*np.pi) / l # Calculate the magnitude of wave-vector

    kx = kmag * np.sin(angle) # Calculate x component of wave-vector
    kz = kmag * np.cos(angle)# Calculate z component of wave-vector

    # scale lx (domain width) to ensure periodicity
    if angledeg in [0, 90, 180]:
        lx = l
    else:
        lx = l / abs(np.sin(angle))



    ##### Parameters #####

    Lx, Lz = num*lx, H
    # Domain size, multiplying by num ensures centre of domain
    is porosity band maximum
```

```
Nx, Nz = 180, 180 # Number of modes in x and z
dealias = 3/2 # Pad modes when transforming to grid space
dtype = np.float64



##### Bases #####

coords = d3.CartesianCoordinates('x', 'z')
# Setting up coordinate system
dist = d3.Distributor(coords, dtype=dtype)
# For Parallelisation, which I did not do
xbasis = d3.RealFourier(coords['x'], size=Nx, bounds=(0, Lx), dealias=dealias)
# Create basis for calculations in x axis
zbasis = d3.ChebyshevT(coords['z'], size=Nz, bounds=(-Lz/2 , Lz/2),
dealias=dealias) # Create basis for calculations in z axis
xbasisd = d3.RealFourier(coords['x'], size=round(Nx*dealias), bounds=(0, Lx))
# Create basis for plotting in x axis
zbasisd = d3.ChebyshevT(coords['z'], size=round(Nz*dealias), bounds=(-Lz/2 , Lz/2))
# Create basis for plotting in z axis



##### Fields #####

p = dist.Field(name='p', bases=(xbasis,zbasis)) # Pressure field
u = dist.VectorField(coords, name='u', bases=(xbasis,zbasis))
```

```
# Perturbation velocity field
Inpor = dist.Field(name='Inpor', bases=(xbasis,zbasis))
# Constant background porosity field
por = dist.Field(name='por', bases=(xbasis,zbasis))
# Perturbation Porosity Field
tau_p = dist.Field(name = 'tau_p')
# Tau term for gauge condition
tau_u1 = dist.VectorField(coords, name='tau_u1', bases=xbasis)
# Tau terms for velocity
tau_u2 = dist.VectorField(coords, name='tau_u2', bases=xbasis)
# Tau terms for velocity
tau_p1 = dist.Field(name='tau_p1', bases=xbasis)# Tau terms for pressure
tau_p2 = dist.Field(name='tau_p2', bases=xbasis)# Tau terms for pressure
c = dist.Field(name='c', bases=(xbasis,zbasis)) # Divergence Field
s = dist.Field(name='s', bases=(xbasis,zbasis)) # Growth rate field



##### Substitutions #####

x, z = dist.local_grids(xbasis, zbasis) # Create an x-z grid
ex, ez = coords.unit_vector_fields(dist) # Unit vectors
lift_basis = zbasis.derivative_basis(1)
#  Creates a derivative basis to apply tau_terms
lift = lambda A: d3.Lift(A, lift_basis, -1)
# Function to multiply with mode/element for selected basis,
necessary for enforcing boundary conditions
```

```
dx = lambda A: d3.Differentiate(A, coords['x']) # Partial Derivative in x
dz = lambda A: d3.Differentiate(A, coords['z']) # Partial Derivative in z


Inpor['g'] = bgpor # Set background porosity field to a constant value
por['g'] = A * np.cos(kx*x + kz*z)
# Create imposed sinusoidal perturbation porosity field from wave-vector


# Z Field (Creating a non-constant coefficient for z axis values)
y = dist.Field(bases=zbasis)
y['g'] = z
# Identity Matrix
I = dist.TensorField(coords)
I['g'][0,0] = 1
I['g'][1,1] = 1
# Identity Matrix
J = dist.TensorField(coords)
J['g'][0,1] = 1
J['g'][1,0] = 1

# 1st Order reductions to apply tau terms
grad_u1 =  d3.grad(u) - ez*lift(tau_u1)
grad_u2 =  d3.TransposeComponents(d3.grad(u) - ez*lift(tau_u1))
dzP = dz(p) + lift(tau_p1)
grad_p = dx(p)*ex + dzP*ez
```

```
# Equation Substitutions
porbrac = (1 + por/Inpor)**n
R1 = (compleng/H)**2 # R1 substitutuion
R2 = 5/3 # R2 substitutuion

C = d3.trace(grad_u1) # Divergence of velosty field
srt = (grad_u1 +  grad_u2 -(2/3)*C*(I)) # Deviaoric strain rate tensor
eta = eta0 * np.exp(-Lam*(por)) # Porosity perturbation dependent shear viscosity

D_phi = D0*eta # Dilatancy prefactor

# Particle Stress Anisotropy
PSA = dist.TensorField(coords)
PSA['g'][0,0] = 1
PSA['g'][1,1] = lamper

srtr = (0.5 * (J + d3.grad(u) +  d3.TransposeComponents(d3.grad(u))
- (2/3)*d3.div(u)*(I))) # Strain rate tensor for RHS
# Convert components to individual fields
srtr_xx = srtr@ex@ex
srtr_xy = srtr@ex@ez
srtr_yx = srtr@ez@ex
srtr_zz = srtr@ez@ez

# Calculate second invariant
I2 = np.sqrt((srtr_xx**2 + srtr_zz**2 + srtr_xy**2 + srtr_yx**2)/2)
```

```
# Calculate dilatancy stress
Dterm = D_phi*PSA*I2



##### Solvers #####

# The code below is how the equations are inputted into the solver,
with the variables needing to be calculated stated top-most line
# LHS contains linear terms, RHS contains non-linear terms
problem1 = d3.NLBVP([p, u, tau_u1, tau_u2, tau_p1, tau_p2, tau_p], namespace=locals(
problem1.add_equation("-C + R1 * div(porbrac * grad_p) + lift(tau_p2) +
tau_p = 0")  # Compaction Equation froma modified Darcy's Law
problem1.add_equation("-grad_p + div(eta * srt) + R2*grad(C)
+ lift(tau_u2) = -div(eta*J) + div(Dterm) ") # Two phase Stokes equation
problem1.add_equation("u(z= Lz/2) = 0*ex + 0*ez")
# Perturbation velocity boundary condition
problem1.add_equation("u(z= -Lz/2) = 0*ex + 0*ez")
# Perturbation velocity boundary condition
problem1.add_equation("(grad_p@ez)(z= Lz/2) = 0")
# Pressure boundary condition
problem1.add_equation("(grad_p@ez)(z= - Lz/2) = 0")
# Pressure boundary condition
problem1.add_equation("integ(p) = 0")
# Gauge condition to create a sparse linear system on LHS

# Setting up solver to solve equations in problem1
```

```
    solver1 = problem1.build_solver(ncc_cutoff=5e-3)
    solver1.newton_iteration()

    # Calculate divergence from velocity field
    problem2 = d3.LBVP([c], namespace=locals())
    problem2.add_equation("c = div(u)")

    solver2 = problem2.build_solver()
    solver2.solve()

    # A too convoluted way of extracting calcualting growth rate
    c_center_row = dist.Field(name='c_center_row', bases=(xbasis,zbasis))
    # Create field to extract central C values
    center_row = round(Nx / 2) # Find central C value
    center_col = round(Nz / 2)  # Find central C value
    c_center_row['g'] = c['g'][center_row,center_col] # Extract central c value
    c_ave = d3.Average(c_center_row, ('x','z')) # Make sure it is a single value
    c_avex = c_ave.evaluate()['g']
    s_calc[i] = c_avex*(1-bgpor)/A # Calculate growth rate
    print(s_calc[i]) # For tracking

    angleangle[i] = angledeg # Prepare to plot correct growth rate at correct angle


# Analytical model
zetain = (5/3)*eta0  # Reference compaction viscosity
nu = (zetain/eta0) + 4/3 # Augmented compaction viscosity ()= 3)
```

```
gammadot = 1  # Strain rate
theta = np.arange(181) # Create range of values for plotting
thetarad = theta*np.pi/180 # Convert to radians

numerator =  (np.sin(thetarad)**2 + lamper*np.cos(thetarad)**2)*np.sin(2*thetarad)**2
denominator = 1-(D0/4)*(1 - lamper)*np.sin(4*thetarad)

sdot1 = (1-bgpor)* ((Lam*gammadot)/3) * ((((kmag)**2))/((1/(R1)**2
+ (kmag)**2)))* (np.sin(2*thetarad) - (D0/2) * (numerator/denominator))
# Calculate growth rate



### Plotting ####

fig, ax = plt.subplots()

ax.axhline(y=0, color = 'grey', linestyle = '--', alpha = 0.2)
ax.plot(theta, sdot1, color='r', alpha= 0.4, label='Analytical Solution')
ax.plot(angleangle, s_calc, color='b', linewidth = '0', marker ='o',
alpha= 0.7,  label='Numerical Solution')
plt.title(f'Scaled Growth Rate at Set Angles ($D_0$ = {D0:.0f},
$_\perp$ = {lamper:.1f})')
plt.xlabel('Angle From Horizontal(°)')
plt.ylabel("Scaled Growth Rate, $\dot{s}$'")
plt.legend(loc = 'lower left')
```

```
plt.savefig(f'benchmark__{D0:.0f}_{lamper:.1f}.png', dpi=200)
plt.clf()
```

## 8.2 Example Code for Melt Evolution Model

```
"""
Code to model the shearing of two-phase dilatant partially molten rock.
"""


import numpy as np
import h5py
import dedalus.public as d3
import matplotlib.pyplot as plt


eta0 = 1 # Reference shear viscosity
Lam = 27 # Porosity dependent shear viscosity exponent
bgpor = 0.05 # Background porosity
n = 3 # Permeability exponent
A = 0.0001 # Amplitude of perturbation
H = 1 # Reference height of domain
compleng = H/4 # Compaction length
D0 = 2 # Dilatancy Factor
lamper =  1 # Particle Stress Anisotropy (Perpendicular)


timestepper = d3.CNAB2 # Timestepper used for IVP
timestep = 0.01 # Timestep progressed by each iteration
stop_sim_time = 1.5+timestep # Duration of model run
numtimesteps = round((stop_sim_time/timestep)) # Number of iterations done
```

```
##### Parameters #####

Lx, Lz = 1, H # Domain Size
Nx, Nz = 32, 32 # Number of modes in x and z
dealias = 3/2 # Pad modes when transforming to grid space
dtype = np.float64


##### Bases #####

coords = d3.CartesianCoordinates('x', 'z') # Setting up coordinate system
dist = d3.Distributor(coords, dtype=dtype)
# For Parallelisation, which I did not do
xbasis = d3.RealFourier(coords['x'], size=Nx, bounds=(0, Lx), dealias=dealias)
# Create basis for calculations in x axis
zbasis = d3.ChebyshevT(coords['z'], size=Nz, bounds=(-Lz/2 , Lz/2), dealias=dealias)
# Create basis for calculations in z axis
xbasisd = d3.RealFourier(coords['x'], size=round(Nx*dealias), bounds=(0, Lx))
# Create basis for plotting in x axis
zbasisd = d3.ChebyshevT(coords['z'], size=round(Nz*dealias), bounds=(-Lz/2 , Lz/2))
# Create basis for plotting in z axis


##### Fields #####
```

```
p = dist.Field(name='p', bases=(xbasis,zbasis))
# Pressure field
u = dist.VectorField(coords, name='u', bases=(xbasis,zbasis))
# Perturbation velocity field
Inpor = dist.Field(name='Inpor', bases=(xbasis,zbasis))
# Constant background porosity field
por = dist.Field(name='por', bases=(xbasis,zbasis))
# Perturbation Porosity Field
tau_p = dist.Field(name = 'tau_p')
# Tau term for gauge condition
tau_u1 = dist.VectorField(coords, name='tau_u1', bases=xbasis)
# Tau terms for velocity
tau_u2 = dist.VectorField(coords, name='tau_u2', bases=xbasis)
# Tau terms for velocity
tau_p1 = dist.Field(name='tau_p1', bases=xbasis)
# Tau terms for pressure
tau_p2 = dist.Field(name='tau_p2', bases=xbasis)
# Tau terms for pressure
tau_por = dist.Field(name = 'tau_por')
# Tau term for gauge condition


##### Setup #####

x, z = dist.local_grids(xbasis, zbasis) # Create an x-z grid
ex, ez = coords.unit_vector_fields(dist) # Unit vectors
lift_basis = zbasis.derivative_basis(1)
```

```
#  Creates a derivative basis to apply tau_terms
lift = lambda A: d3.Lift(A, lift_basis, -1)
# Function to multiply with mode/element for selected basis,
necessary for enforcing boundary conditions
dx = lambda A: d3.Differentiate(A, coords['x']) # Partial Derivative in x
dz = lambda A: d3.Differentiate(A, coords['z']) # Partial Derivative in z

Inpor['g'] = bgpor # Set background porosity field to a constant value
por.fill_random('g', seed=42, distribution='normal', scale=A)
# Create random perturbation porosity field
por['g'] *= A/np.max(np.abs(por['g']))
# Normalise perturbed porosity field to be between set values

u['g'][0] = 0 # Set inital horizontal velocity to 0
u['g'][1] = 0 # Set inital vertical velocity to 0

snapshot = np.zeros((round(Nx*dealias),round(Nz*dealias), numtimesteps))
# Create grid which can be saved as HDF5 file for subsequent processing


##### Model #####

for i in range(0, numtimesteps):
# Progress the model for the number of timesteps required


##### Substitutions #####
```

```
# Z Field (Creating a non-constant coefficient for z axis values)
y = dist.Field(bases=zbasis)
y['g'] = z
# Identity Matrix
I = dist.TensorField(coords)
I['g'][0,0] = 1
I['g'][1,1] = 1
# Identity Matrix
J = dist.TensorField(coords)
J['g'][0,1] = 1
J['g'][1,0] = 1

# 1st Order reductions to apply tau terms
grad_u1 =  d3.grad(u) - ez*lift(tau_u1)
grad_u2 =  d3.TransposeComponents(d3.grad(u) - ez*lift(tau_u1))
dzP = dz(p) + lift(tau_p1)
grad_p = dx(p)*ex + dzP*ez

# Equation Substitutions
porbrac = (1 + por/Inpor)**n
R1 = (compleng/H)**2 # R1 substitutuion
R2 = 5/3 # R2 substitutuion

C = d3.trace(grad_u1) # Divergence of velosty field
srt = (grad_u1 +  grad_u2 -(2/3)*C*(I)) # Deviaoric strain rate tensor
eta = eta0 * np.exp(-Lam*(por)) # Porosity perturbation dependent shear viscosity
```

```
D_phi = D0*eta # Dilatancy prefactor


# Particle Stress Anisotropy
PSA = dist.TensorField(coords)
PSA['g'][0,0] = 1
PSA['g'][1,1] = lamper


srtr = (0.5 * (J + d3.grad(u) +  d3.TransposeComponents(d3.grad(u))
- (2/3)*d3.div(u)*(I))) # Strain rate tensor for RHS
I1 = d3.Trace(srtr)
# Convert components to individual fields
srtr_xx = srtr@ex@ex
srtr_xy = srtr@ex@ez
srtr_yx = srtr@ez@ex
srtr_zz = srtr@ez@ez
# Calculate trace of squared tensor


# Calculate second invariant
I2 = np.sqrt((srtr_xx**2 + srtr_zz**2 + srtr_xy**2 + srtr_yx**2)/2)


# Calculate dilatancy stress
Dterm = D_phi*PSA*I2



##### Solvers #####
```

```
# The code below is how the equations are inputted into the solver,
with the variables needing to be calculated stated top-most line
# LHS contains linear terms, RHS contains non-linear terms
problem1 = d3.NLBVP([p, u, tau_u1, tau_u2, tau_p1, tau_p2, tau_p],
namespace=locals())
problem1.add_equation("-C + R1 * div(porbrac * grad_p) + lift(tau_p2)
+ tau_p = 0") # Compaction Equation froma modified Darcy's Law
problem1.add_equation("-grad_p + div(eta * srt) + R2*grad(C)
+ lift(tau_u2) = -div(eta*J) + div(Dterm) ") # Two phase Stokes equation
problem1.add_equation("u(z= Lz/2) = 0*ex + 0*ez")
# Perturbation velocity boundary condition
problem1.add_equation("u(z= -Lz/2) = 0*ex + 0*ez")
# Perturbation velocity boundary condition
problem1.add_equation("(grad_p@ez)(z= Lz/2) = 0")
# Pressure boundary condition
problem1.add_equation("(grad_p@ez)(z= - Lz/2) = 0")
# Pressure boundary condition
problem1.add_equation("integ(p) = 0")
# Gauge condition to create a sparse linear system on LHS

# Setting up solver to solve equations in problem1
solver1 = problem1.build_solver(ncc_cutoff=5e-3)
solver1.newton_iteration()

# Calculate resulting porosity field using porsity evolution equation
problem2 = d3.IVP([por, tau_por], namespace=locals())
problem2.add_equation("dt(por) + (y*ex + u)@grad(por) + por*div(u)
```

```
+ tau_por = (1-Inpor)*div(u)")
problem2.add_equation("integ(por) = 0")

# Solve probelem2 to calculate porosity field
solver2 = problem2.build_solver(timestepper)
solver2.stop_sim_time = timestep
solver2.step(timestep)

print(i)


##### Plotting #####

# Create dealias grids
x_dealias, z_dealias = dist.local_grids(xbasisd, zbasisd)

# Add background porosity to perturbation field to get total porosity
port = dist.Field(name='port', bases=(xbasisd, zbasisd))
port['g'] = por['g'] + bgpor

# Update Snapshot so it can be saved as hdf5 file later
snapshot[:, :, i] = port['g']

# Gather for plotting (global array, if using MPI)
porg = port.allgather_data('g')

# Create meshgrid from x and z (use meshgrid for 2D data alignment)
```

```
    X, Z = np.meshgrid(x_dealias, z_dealias, indexing='ij')

    # Set up plot
    fig, ax = plt.subplots()

    # Plot colourmap using
    por_plot = ax.pcolormesh(X, Z, porg, cmap='viridis',
    shading='gouraud', rasterized=True)

    # Set axis titles, labels and axis ratios
    ax.set_title('Porosity', loc='left')
    ax.set_title(f'$D_0$ = {D0:.0f}   $_\\perp$ = {lamper:.1f}
    $\\gamma$ = {(i*timestep):.2f}', alpha=0.5, loc='right')
    fig.colorbar(por_plot, ax=ax)
    ax.set_aspect('auto')
    ax.set_xlabel('x')
    ax.set_ylabel('z')

    # Save plot
    plt.savefig(f'IVP__{D0:.0f}_{lamper:.1f}_{i:.0f}.png', dpi=200)
    plt.close(fig)
    plt.clf()


##### Saving #####

# Save HDF5 file for later processing or plotting
```

```python
with h5py.File(f'porosity_{D0:.0f}_{lamper:.1f}.h5', 'w') as f:

    f.create_dataset('field_data', data=snapshot)
```

## 8.3 Additional Spectral Analysis of Dilatancy Bands

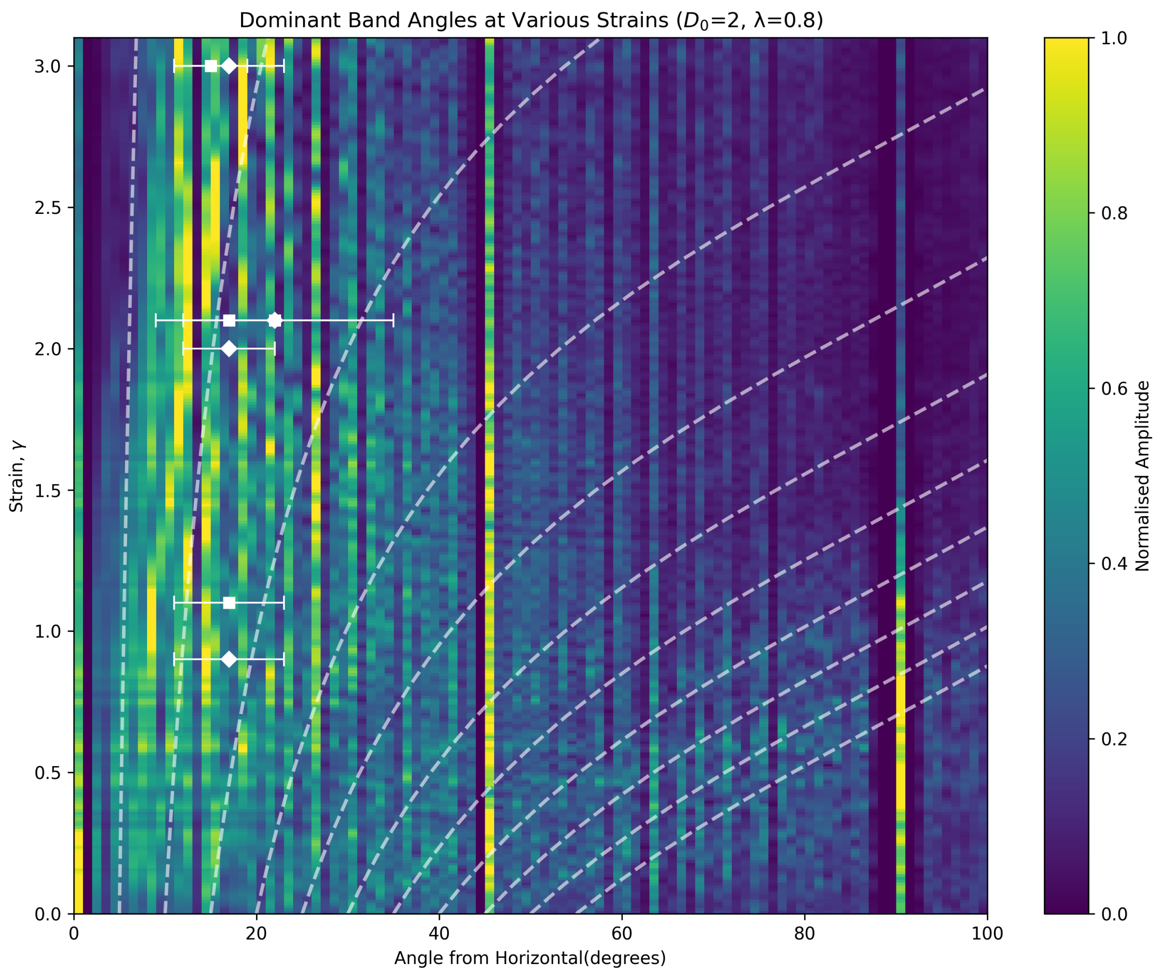


Figure 18: Spectral dataset showing how dominant band angles evolve with strain when $D_0 = 2$ and $\Lambda_\perp = 0.8$. The white dotted lines are the passive advection trajectories of bands from simple shear, taken from Katz (2022). The white markers are band angles calculated from PMR simple shear experiments. The squares are from Holtzman et al. (2003) and the rhombi are from Holtzman et al. (2007). The dominant band angles matche experiments well and is similar to when $D_0 = 2$ and $\Lambda_\perp = 1.0$ shown in Figure 14.

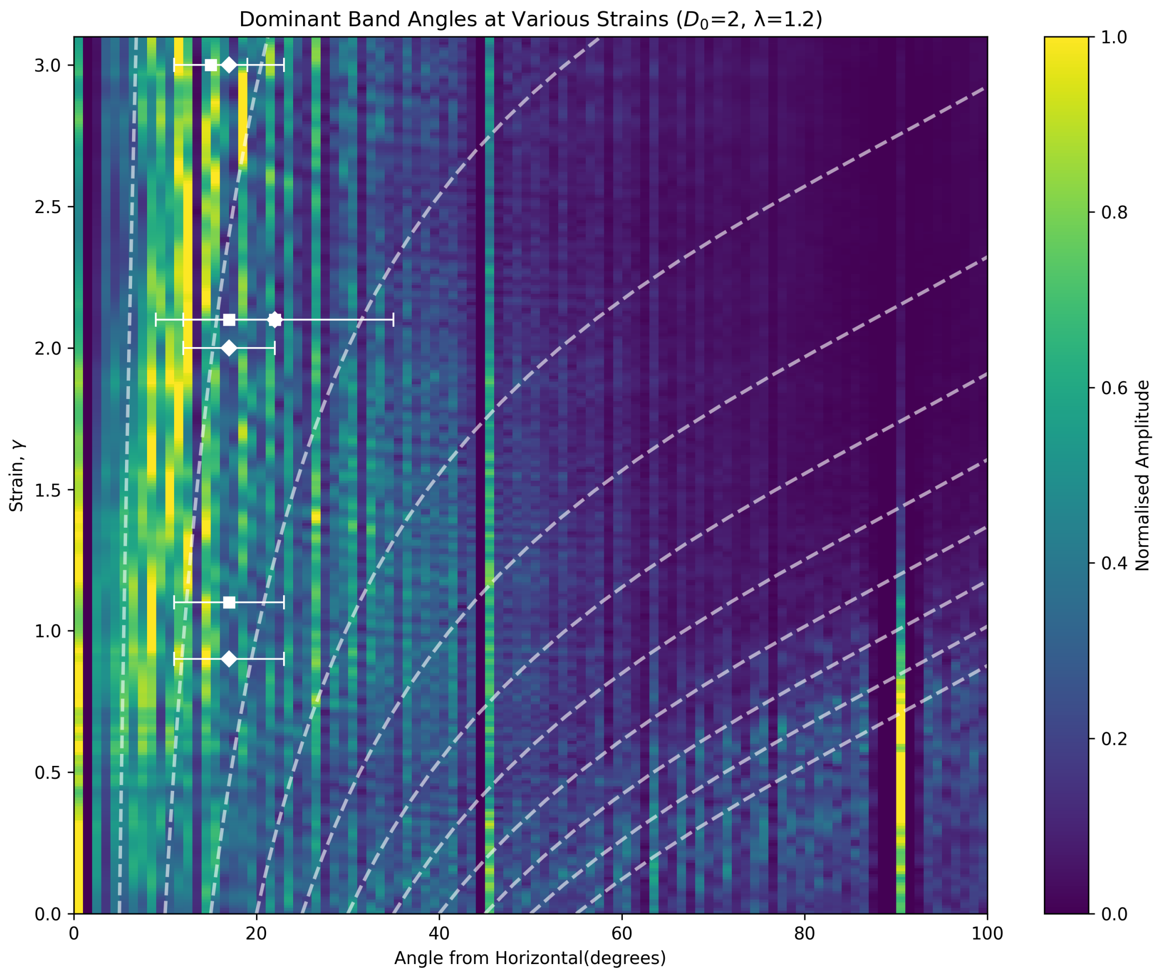


Figure 19: Spectral dataset showing how dominant band angles evolve with strain when $D_0 = 2$ and $\Lambda_\perp = 1.2$. The white dotted lines are the passive advection trajectories of bands from simple shear, taken from Katz (2022). The white markers are band angles calculated from PMR simple shear experiments. The squares are from Holtzman et al. (2003) and the rhombi are from Holtzman et al. (2007). The dominant band angles are slightly shallower than the experiments.

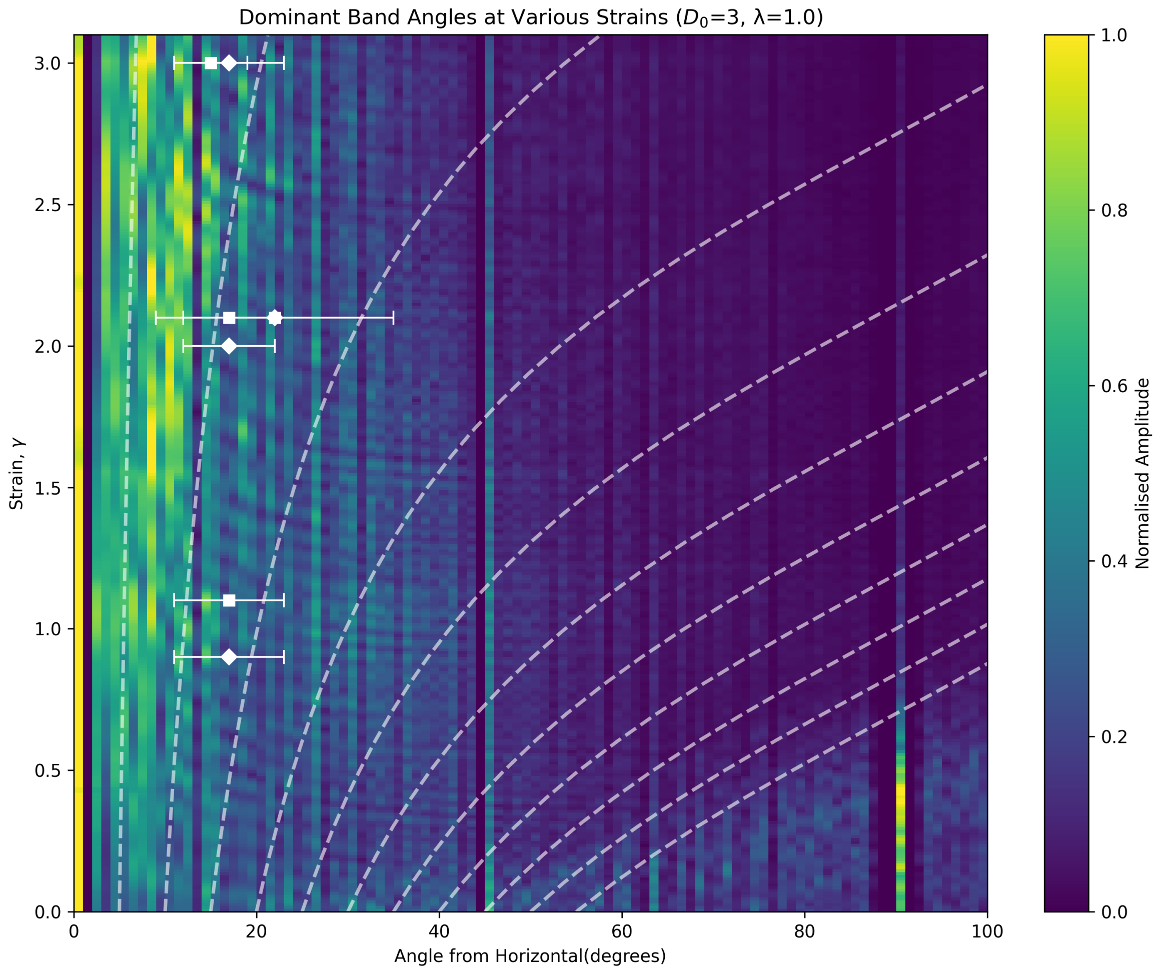


Figure 20: Spectral dataset showing how dominant band angles evolve with strain when $D_0 = 3$ and $\Lambda_\perp = 1.0$. The white dotted lines are the passive advection trajectories of bands from simple shear, taken from Katz (2022). The white markers are band angles calculated from PMR simple shear experiments. The squares are from Holtzman et al. (2003) and the rhombi are from Holtzman et al. (2007). The dominant band angles are much lower than the experiments.

## 8.4 Varying Poiseuille Flow Parameters

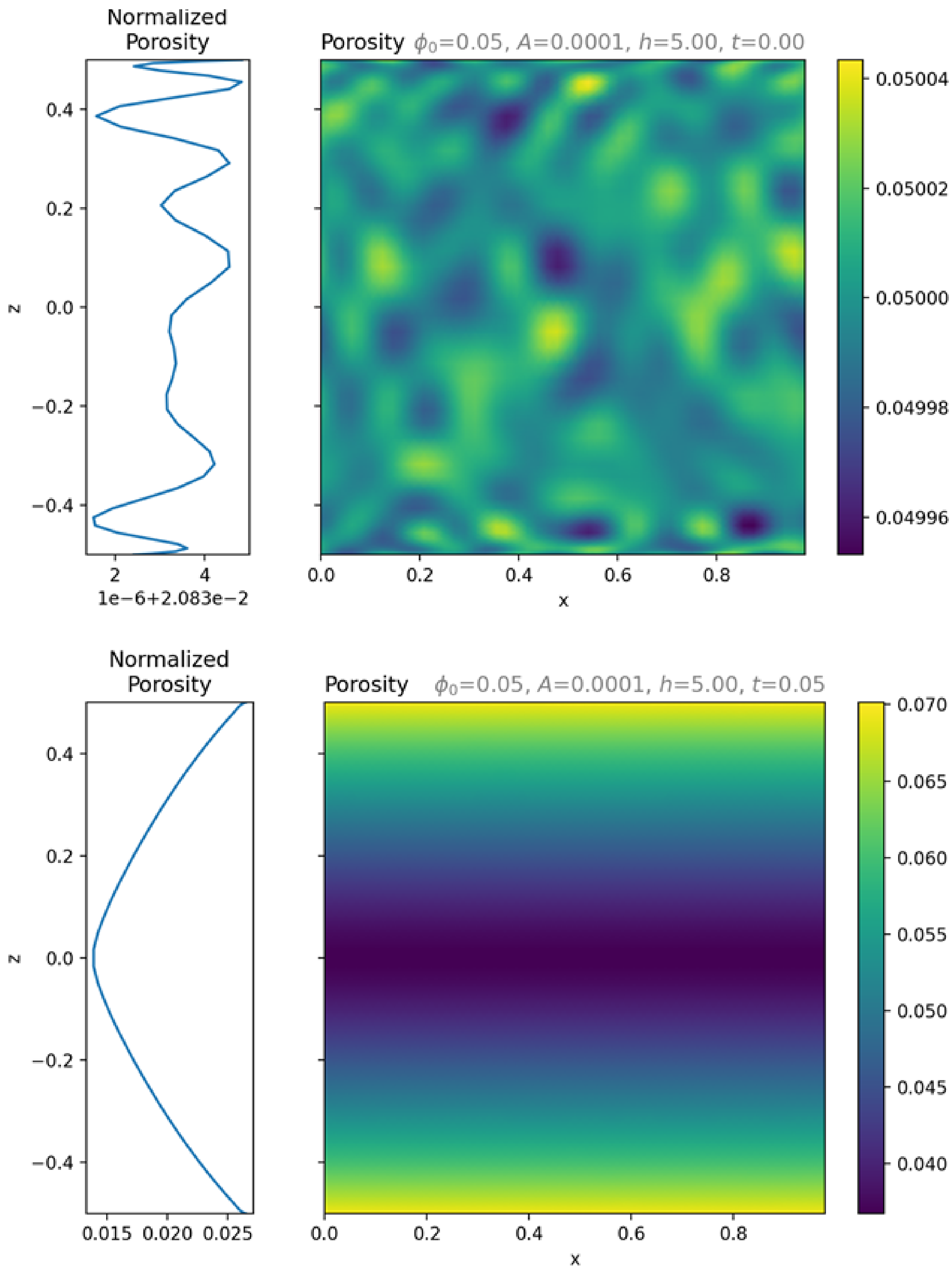


Figure 21: Simulation with a large forcing and small porosity perturbation showing the porosity being redistributed to the margins of the model. Low-angle melt-rich bands are not preserved.

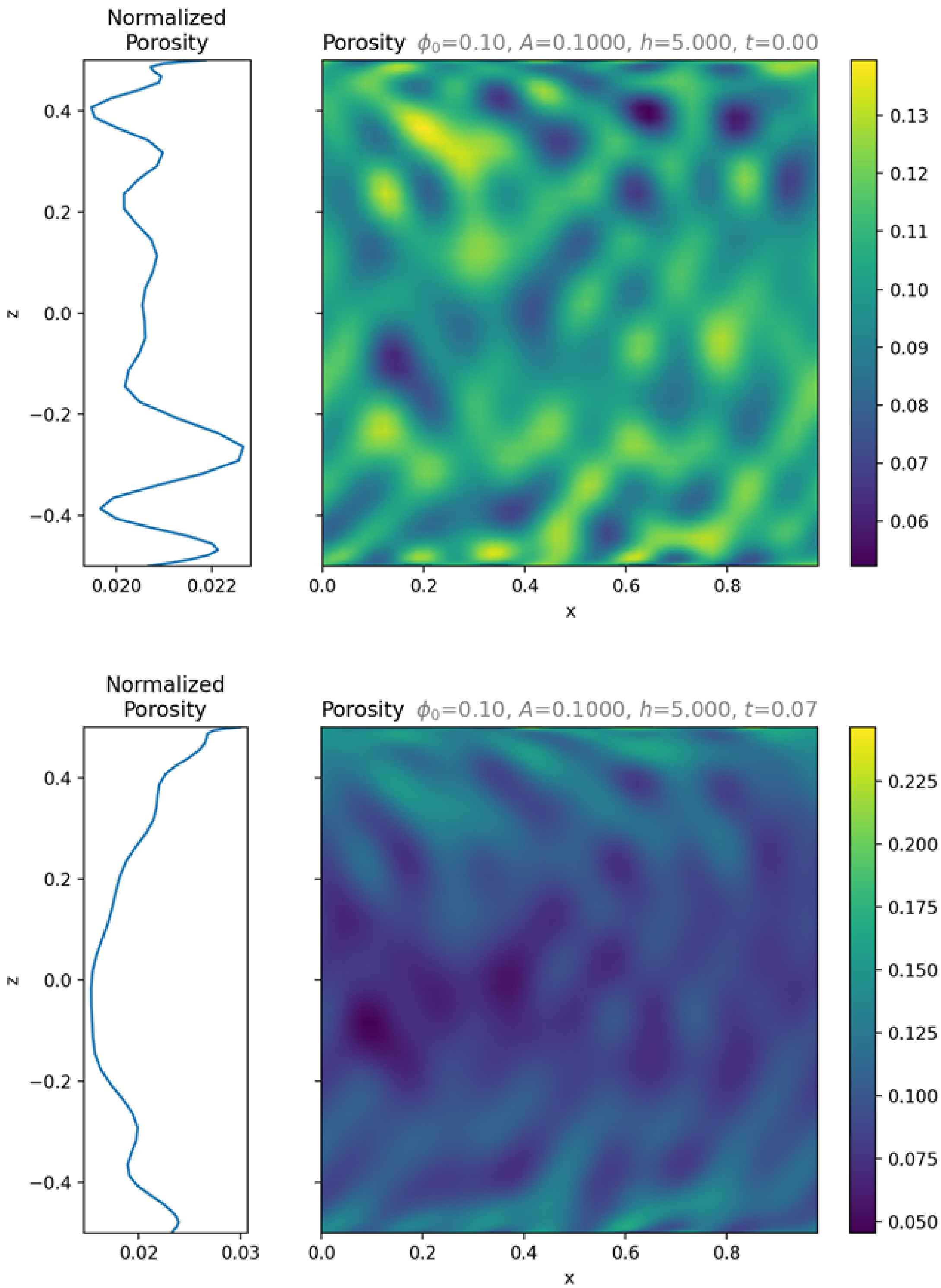


Figure 22: Simulation with a large forcing and porosity perturbation showing the preservation of subtle melt-rich bands.

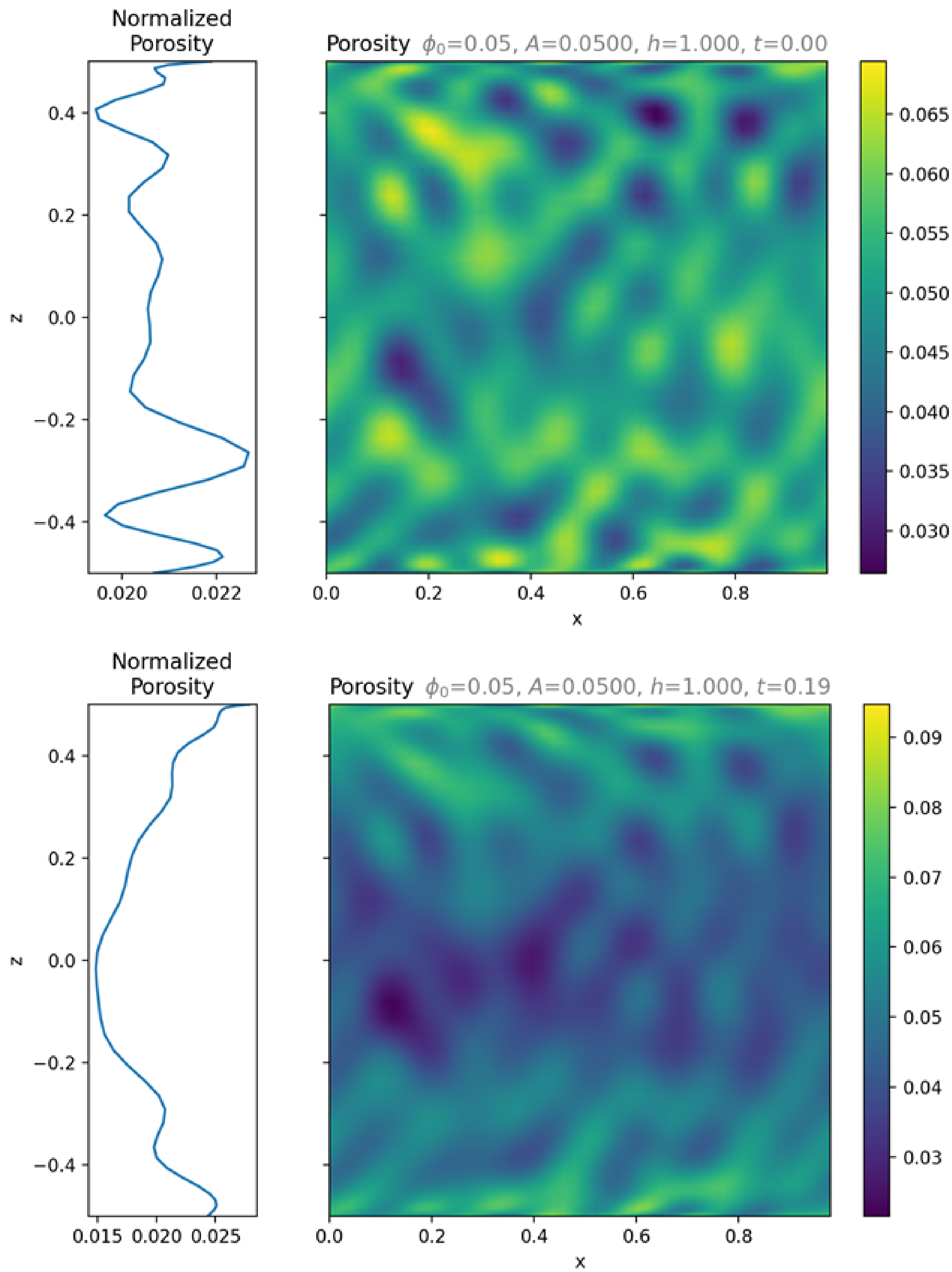


Figure 23: Simulations with a medium porosity perturbation and medium forcing showing the slight preservation of subtle melt-rich bands.

## 8.5 Dyke Chemistry Data

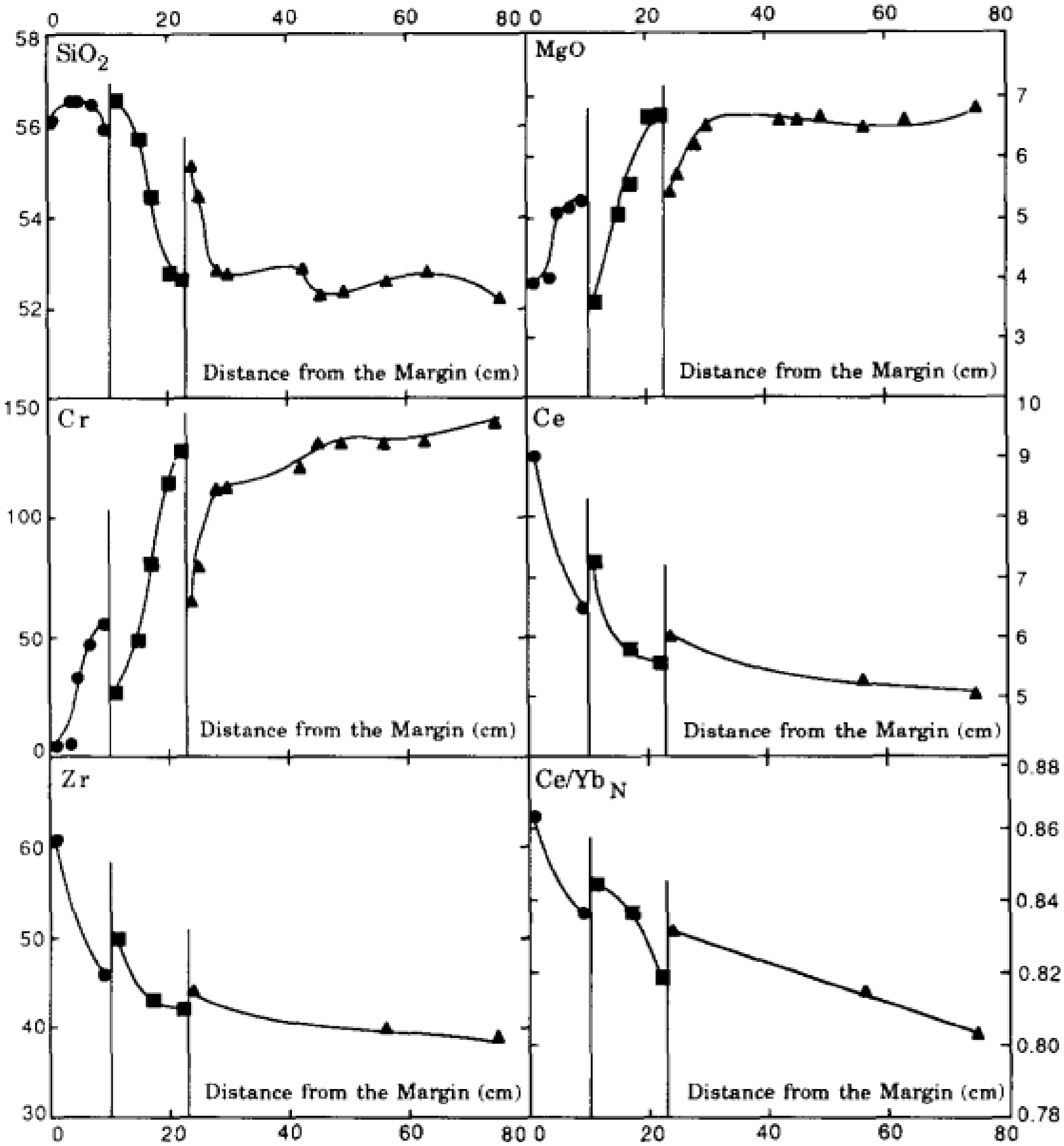


Figure 24: Data from Brouxel (1991) showing elemental concentrations across a dyke transect in the Trinity Ophiolite, Northern California, USA, consistent with more evolved melts at the edges.

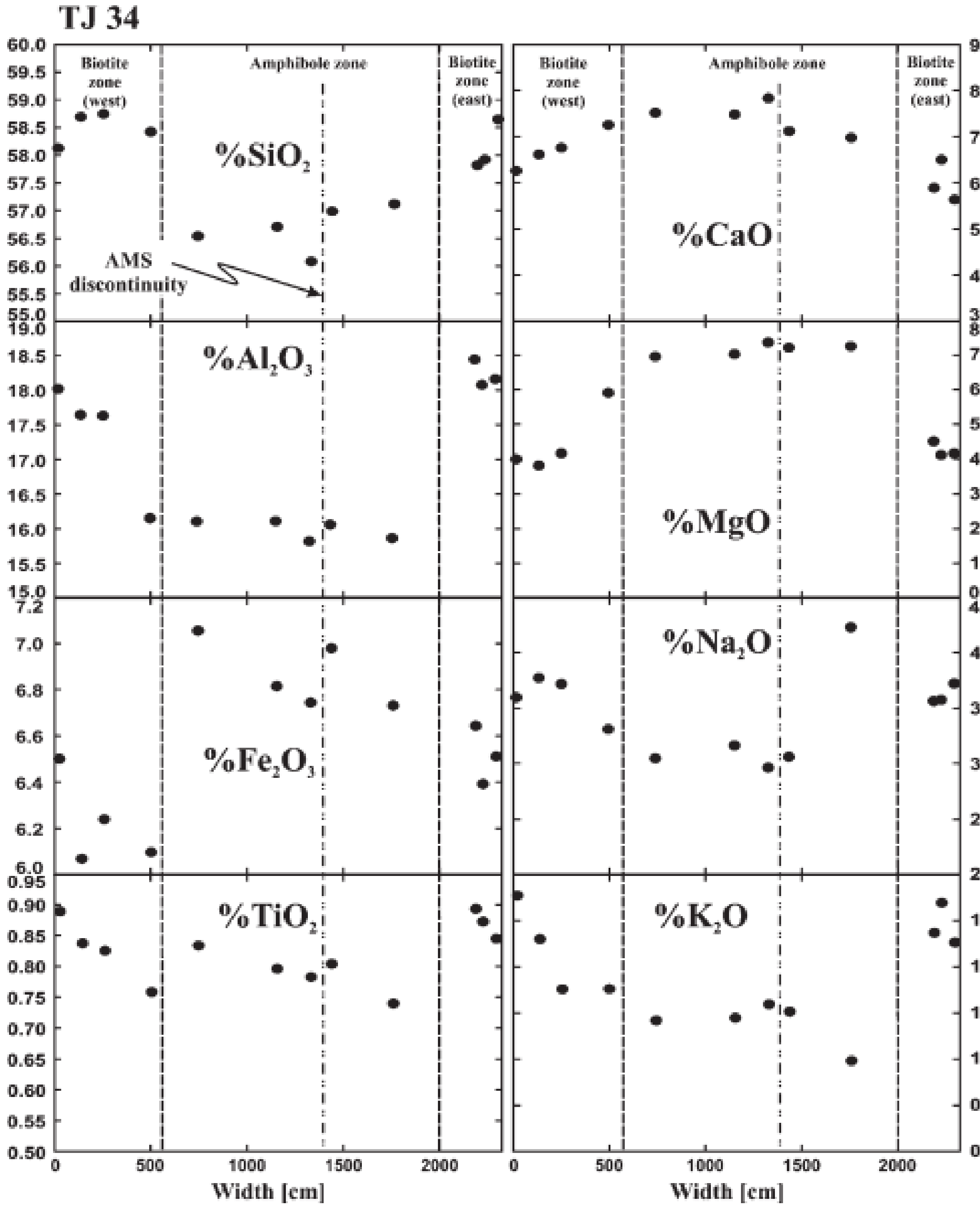


Figure 25: Data from Nkono et al. (2006) showing elemental concentrations across a dyke of the Motru Dyke Swarm, Southern Carpathians, Romania, consistent with more evolved melts at the edges.